

THE FORMATION OF THE FIRST STARS. I. THE PRIMORDIAL STAR FORMING CLOUD

VOLKER BROMM¹, PAOLO S. COPPI AND RICHARD B. LARSON
Department of Astronomy, Yale University, New Haven, CT 06520-8101;
volker@ast.cam.ac.uk, coppi@astro.yale.edu, larson@astro.yale.edu
To appear in ApJ

ABSTRACT

To constrain the nature of the very first stars, we investigate the collapse and fragmentation of primordial, metal-free gas clouds. We explore the physics of primordial star formation by means of three-dimensional simulations of the dark matter and gas components, using smoothed particle hydrodynamics, under a wide range of initial conditions, including the initial spin, the total mass of the halo, the redshift of virialization, the power spectrum of the DM fluctuations, the presence of HD cooling, and the number of particles employed in the simulation. We find characteristic values for the temperature, $T \sim$ a few 100 K, and the density, $n \sim 10^3 - 10^4 \text{ cm}^{-3}$, characterising the gas at the end of the initial free-fall phase. These values are rather insensitive to the initial conditions. The corresponding Jeans mass is $M_J \sim 10^3 M_\odot$. The existence of these characteristic values has a robust explanation in the microphysics of H₂ cooling, connected to the minimum temperature that can be reached with the H₂ coolant, and to the critical density at which the transition takes place between levels being populated according to NLTE, and according to LTE.

In all cases, the gas dissipatively settles into an irregular, central configuration which has a filamentary and knotty appearance. The fluid regions with the highest densities are the first to undergo runaway collapse due to gravitational instability, and to form clumps with initial masses $\sim 10^3 M_\odot$, close to the characteristic Jeans scale. These results suggest that the first stars might have been quite massive, possibly even very massive with $M_\star \gtrsim 100 M_\odot$.

After a gas element has undergone runaway collapse, and has reached densities in excess of 10^8 cm^{-3} , a sink particle is created. This procedure allows us to follow the evolution of the overall system beyond the point where the first nonlinear region would otherwise force the calculation to a halt. These later evolutionary stages, during which the clumps grow in mass due to accretion and merging with other clumps, are quite sensitive to the initial conditions. The key process in building up very massive clumps, with masses up to a few times $10^4 M_\odot$, is merging between clumps. Since the merging rate sensitively depends on the density of the gas, halos with the highest degree of central concentration are able to assemble the most massive clumps. Among these are halos with a low spin ($\lambda \simeq 0.01$), and with DM fluctuations imprinted according to a white-noise spectrum.

Subject headings: cosmology: theory — early universe — galaxies: formation — stars: formation — hydrodynamics

1. INTRODUCTION

This paper is concerned with the initial stages in the formation of cosmic structure. How did the universe evolve from the extreme uniformity of the big bang fireball into its highly organized and clustered present state? An increasing wealth of observational data has become available to guide theoretical thinking. The study of anisotropies in the cosmic microwave background (CMB) provides a window into the earliest phases of structure formation, when the primordial density fluctuations were still linear, and therefore amenable to an exact physical description (e.g., White, Scott, & Silk 1994; Lawrence, Scott, & White 1999). Thus, we have a powerful probe of the last scattering surface at $z \simeq 1000$, corresponding to $\sim 10^6$ yr after the big bang. Complementary to the CMB studies are observations of high-redshift quasars and galaxies (e.g., Hu, Cowie, & McMahon 1998; Chen, Lanzetta, & Pascarelle 1999; Fan et al. 2000). The light from these objects originated at $z \simeq 5$, when the universe was $\sim 10^9$ yr old.

Very little is known about the crucial era in between, at $z = 1000 - 5$, which has been termed the “dark ages” (e.g., Loeb 1999, Rees 1999). This serene epoch ended when the first luminous objects lit up the universe again. In the context of hierarchical scenarios of structure formation, as specified by a variant of the cold dark matter (CDM) model, the collapse of the first baryonic objects is expected at redshifts $z \simeq 50 - 10$, involving dark matter halos of mass $\sim 10^6 M_\odot$ (Tegmark et al. 1997).

The importance of the first stars and quasars derives from the crucial feedback they exert on the intergalactic medium (IGM). A generation of stars which formed out of primordial, pure H/He gas (the so-called Population III) must have existed, since heavy elements can only be synthesized in the interior of stars. Population III stars, then, were responsible for the initial enrichment of the IGM with heavy elements. From the absence of Gunn-Peterson absorption in the spectra of high-redshift quasars, we know that the universe has undergone a reionization event at

¹Present address: Institute of Astronomy, University of Cambridge, Madingley Road, Cambridge CB3 0HA, UK

$z > 5$ (Gunn & Peterson 1965). UV photons from the first stars, perhaps together with an early population of quasars, are expected to have contributed to the reionization of the IGM (Haiman & Loeb 1997; Ferrara 1998; Miralda-Escudé, Haehnelt, & Rees 2000). The energy input from the first stars might have left a measurable imprint on the CMB on very small scales (Vishniac 1987; Dodelson & Jubas 1995).

Despite an intense observational effort, the discovery of a true Population III star remains elusive. Surveys of the metal-poor population in the halo of our Galaxy have resulted in stars with metallicities $Z \gtrsim 10^{-4} Z_{\odot}$ (Beers 2000). Spectroscopic studies of high-redshift Lyman α clouds, the supposedly most pristine objects in the universe, find a minimum metallicity $Z_{min} \sim 10^{-3} Z_{\odot}$ (Cowie & Songaila 1998). Therefore, wherever we look, we find contaminated material. To probe the time when star formation first started, consequently entails observing at even higher redshift. This is the main purpose of the *Next Generation Space Telescope* (NGST) which is designed to reach \sim nJy sensitivity at near-infrared wavelengths (Loeb 1998). In preparation for this upcoming observational revolution, the study of the first stars is very timely, providing a theoretical framework for the interpretation of what NGST might discover, less than a decade from now.

The question arises how one can make any progress in understanding primordial star formation, given the lack of direct observational constraints. The physics of the first stars, however, is characterized by some important simplifications, as compared to the extreme complexity of present-day star formation (Larson 1998; Loeb 1998). The absence of metals, and consequently of dust, leaves atomic and molecular hydrogen as the main agent of radiative cooling and the source of opacity. Magnetic fields were likely to be dynamically insignificant, prior to the onset of efficient (stellar) dynamo amplification (Kulsrud 1997). The chemistry and heating of the primordial gas was not yet complicated by the presence of a UV radiation background. The IGM must have been a rather quiescent place, with no source to sustain turbulent motion, as long as the density perturbations remain in their linear stage. Only after the explosion of the first supernovae, and the associated input of mechanical and thermal energy, is this state of primordial tranquility bound to change (Loeb & Haiman 1997; Miralda-Escudé & Rees 1997). Therefore, the physics of primordial star formation is mainly governed by gravity, thermal pressure, and angular momentum. This situation renders the problem theoretically more straightforward and tractable than the highly complex present-day case which continues to defy attempts to formulate a fundamental theory of star formation. Finally, the initial conditions for the collapse of a primordial star forming cloud are given by the adopted model of cosmological structure formation. The initial abundances of the chemical species are predicted by standard Big-Bang nucleosynthesis (e.g., Copi, Schramm, & Turner 1995).

In this paper, we investigate the question: *How do the first primordial star forming clouds evolve in the context of a hierarchical model of structure formation?* The collapse of the clouds, having masses close to the cosmological Jeans mass ($\sim 10^6 M_{\odot}$), results in the formation of high density clumps. These clumps are the immediate progen-

itor of primordial protostars. This second stage in the primordial star formation process will be discussed in a subsequent paper (henceforth Paper II).

The subject of the formation of the first stars has a long and venerable history (e.g., Yoneyama 1972; Hutchins 1976; Silk 1977, 1983; Carlberg 1981; Kashlinsky & Rees 1983; Palla, Salpeter, & Stahler 1983; Carr, Bond, & Arnett 1984; Couchman & Rees 1986; Haiman, Thoul, & Loeb 1996; Uehara et al. 1996; Tegmark et al. 1997; Omukai & Nishi 1998; Nakamura & Umemura 1999). Recently, it has become possible to address this problem in the context of full cosmological simulations, due to dramatic improvements in numerical resolution, and in the modelling of the relevant gas physics (Anninos & Norman 1996; Ostriker & Gnedin 1996; Abel et al. 1998; Abel, Bryan, & Norman 2000, ABN2000 henceforth; Fuller & Couchman 2000).

Our approach is complementary to these last studies in that we focus on the collapse of an isolated overdensity. This choice has its advantages and shortcomings. Paramount among the latter, we ignore the tidal effects of the large scale matter distribution which are responsible for generating the angular momentum in the collapsing structures. The amount and distribution of angular momentum therefore are free parameters in our simulations. In prescribing them, however, we can draw on the insight from cosmological numerical simulations. These result in a statistical description of the angular momentum (spin) which a given dark matter halo is expected to acquire (e.g., Barnes & Efstathiou 1987). The primary advantage of our method, on the other hand, is that it allows us to comprehensively explore the behavior of the primordial gas under a variety of initial conditions. In doing so, we hope to single out the essential physics, and to test its robustness. In a previous publication, we have already presented first results (Bromm, Coppi, & Larson 1999).

The organization of this paper is as follows. In §2, we discuss the relevant physical ingredients, both for the dark matter and baryonic components. A description of our numerical method is given in §3, whereas §4 presents the results of our exploratory survey. Finally, §5 contains our conclusions and debates avenues for further progress.

2. THE PHYSICAL INGREDIENTS

2.1. *Dark Matter*

Current scenarios of cosmological structure formation assume the dark matter (DM) to be ‘cold’, in the sense of having negligible velocity dispersion. Candidates include the lightest supersymmetric particle, the photino, of estimated mass ~ 100 GeV, and the invisible axion (e.g., Peacock 1999). Primordial density fluctuations in the cold dark matter have consequently survived on all scales due to the absence of free-streaming. Provided these fluctuations obey Gaussian statistics, as predicted by inflation, they are fully described by the power spectrum $P(k)$, with k denoting the wavenumber. The standard CDM model (e.g., Blumenthal et al. 1984) predicts that the fluctuations decrease with mass, leading to a hierarchical (bottom-up) picture of structure formation. Variants of CDM agree qualitatively with each other, and we take the standard CDM model as a convenient template for our discussion. In the critical Einstein-de Sitter model, the rms density

contrast on a mass scale M grows in time according to $\sigma(M) = \sigma_0(M)/(1+z)$, as long as the fluctuation remains in the linear stage. $\sigma_0(M)$ is the linear extrapolation to the present epoch. In a model with a cosmological constant, growth is suppressed at recent epochs ($z < 10$), but at earlier times, the simple Einstein-de Sitter behavior still applies. For a DM halo of given mass M , corresponding to a $\nu\sigma$ -peak in the Gaussian random field, the redshift of collapse can be estimated as

$$1 + z_{vir} = \frac{\nu\sigma_0(M)}{\delta_c} . \quad (1)$$

The threshold overdensity for collapse is often taken to be $\delta_c = 1.69$ (Peacock 1999). We discuss in Section 2.3 that the first stars are expected to form in DM halos of mass $\sim 10^6 M_\odot$, corresponding to $3 - 4\sigma$ peaks. At these small scales, halos of increasing mass collapse in rapid succession. This (‘cross-talk’) behavior is characteristic of the CDM model (Rees 2000). The CDM power spectrum approaches $P(k) \propto k^{-3}$ asymptotically on small scales. This is characteristic for the DM fluctuations within a Population III star forming region. Since the baryonic mass is smaller than the initial Jeans mass, all perturbations in the gas have been wiped out by pressure forces. The presence of the small-scale DM fluctuations, therefore, might play an important role in shaping the fate of the collapsing gas.

A collapsing DM halo is expected to acquire angular momentum via tidal interactions with neighboring overdensities. The outcome of this process can be conveniently described by the dimensionless spin parameter

$$\lambda = \frac{L|E|^{1/2}}{GM^{5/2}} , \quad (2)$$

where L , E , and M are the total angular momentum, energy, and mass, respectively, with G being Newton’s constant. Numerical simulations result in an average spin parameter of $\lambda \simeq 0.05$ (e.g., Barnes & Efstathiou 1987).

Once a perturbation on a given mass scale reaches overdensities $\delta = (\rho_{halo} - \rho_b)/\rho_b$ of close to unity, with ρ_b being the density of the unperturbed background universe, the linear description breaks down, and the halo is undergoing nonlinear collapse. A convenient analytical model for the nonlinear evolution of DM halos is given by the spherical top-hat model (e.g., Padmanabhan 1993). At redshifts close to z_{vir} , the DM particles reach a state of virial equilibrium. The approach to virial equilibrium occurs through the process often called violent relaxation in the literature (Lynden-Bell 1967). This process operates on a dynamical timescale, as opposed to the slow two-body relaxation. The halo density after virialization is estimated to be

$$\rho_{vir} \simeq 18\pi^2 \rho_b = 18\pi^2 \rho_0 (1 + z_{vir})^3 , \quad (3)$$

where $\rho_0 = 1.88 \times 10^{-29} \text{ g cm}^{-3} \Omega_m h^2$ is the density of the present-day universe. The baryons partake in the DM collapse, and acquire, through shocks and adiabatic compression, the virial temperature

$$T_{vir} \simeq \frac{GMm_H}{2R_{vir}k_B} \simeq 100 \text{ K} h^{2/3} \left(\frac{M}{10^6 M_\odot} \right)^{2/3} (1 + z_{vir}) . \quad (4)$$

Here, R_{vir} denotes the virial radius, k_B is Boltzmann’s constant, and m_H is the mass of a hydrogen atom. Although realistic DM halos are much more complicated than this simple model, the top-hat results give an intuitive way to understand the physics of complex situations to within factors of a few. It also allows us to specify the initial conditions for our numerical simulations (see Section 4).

In Figure 1, we show the density evolution of a top-hat perturbation, and compare the analytical prediction with the result of one of our numerical simulations. It can be seen that the prediction of ρ_{vir} in equ. (3) is nicely reproduced in the simulation, after an epoch of settling down to the equilibrium state.

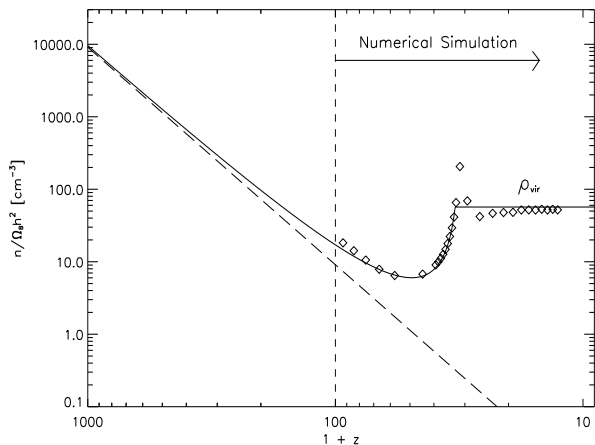


FIG. 1.— Top-hat model for an overdensity collapsing at $z_{vir} \simeq 30$. Shown is the number density of hydrogen atoms vs. redshift. *Solid line*: Density evolution according to top-hat solution. *Long-dashed line*: Density evolution in the expanding background (E-dS) universe. ρ_{vir} denotes the ‘virial plateau’, the estimated density after violent relaxation has established virial equilibrium. *Diamond-shaped symbols*: Evolution of the average gas density in adiabatic test case. The simulation is initialized at $z = 100$ to reproduce the top-hat collapse. As can be seen, the agreement with the analytical solution is good. Notice also that the average gas density settles eventually to a value close to ρ_{vir} .

2.2. Baryons

The fate of the baryons is determined by the strife between gravity and opposing pressure, and it is, therefore, essential to understand the thermal history of the gas, a topic which we address in the following subsection.

2.2.1. Cooling and Heating

The thermal evolution of the gas is governed by the equation:

$$\frac{Du}{Dt} = \frac{P}{\rho^2} \frac{D\rho}{Dt} + \frac{\Gamma - \Lambda}{\rho} \quad (5)$$

Here, P and ρ are the gas pressure and density, u is the specific internal energy (in erg g^{-1}), and Γ and Λ are the contributions from radiative heating and cooling, respectively. The first term on the right-hand side describes adiabatic cooling due to expansion or heating due to compression. We now discuss the relevant processes of radiative cooling.

In the absence of metals, H_2 is the main coolant below $\sim 10^4$ K, which is the temperature range typically encountered in collapsing Population III objects. Being homonu-

clear, H_2 possesses no permanent dipole moment. Rotational transitions, therefore, can only occur via electric quadrupole radiation with the corresponding very small transition probabilities ($A \sim 10^{-11} \text{ s}^{-1}$ for the lowest-lying transition). The H_2 cooling function has been investigated by a number of authors whose results, however, differed by up to a factor of 100 (Hollenbach & McKee 1979; Lepp & Shull 1983). A crucial uncertainty concerned the low temperature (a few 100 K) regime, where quantum-mechanical effects were not yet taken into proper account. Recently, the cooling rates have been thoroughly recomputed. We have implemented H_2 cooling using the new parameterization of Galli & Palla (1998). These authors have included improved collisional rates for $T > 600$ K (Martin, Schwarz, & Mandy 1996), as well as for $T < 600$ K (Forrey et al. 1997), and have assumed ortho- and para- H_2 to be present in their equilibrium ratio of 3:1. In general, the cooling rate (in $\text{erg s}^{-1} \text{ cm}^{-3}$) can be written as

$$\Lambda = \sum_{u \rightarrow l} n_u A_{ul} \Delta E_{ul} \quad , \quad (6)$$

where the sum extends over all possible transitions $u \rightarrow l$. A_{ul} is the Einstein coefficient for spontaneous emission, ΔE_{ul} the respective energy difference, and n_u the density of H_2 in the (upper) level u . In the low-density regime ($n \rightarrow 0$), each collisional excitation is almost instantaneously followed by spontaneous emission. The level populations are then determined by the rate of H- H_2 collisions:

$$n_u^{(n \rightarrow 0)} \propto n_{\text{H}_2} n_{\text{H}} \gamma_{lu} \propto n_{\text{H}}^2 \quad , \quad (7)$$

with γ_{lu} being the coefficient of collisional excitation. At high density, the levels are populated according to LTE:

$$n_u^{(\text{LTE})} \propto n_{\text{H}} \exp(-\Delta E_{ul}/k_B T) \propto n_{\text{H}} \quad . \quad (8)$$

Summarizing the limiting behavior, one has:

$$\Lambda \rightarrow \begin{cases} \Lambda^{(n \rightarrow 0)} \propto n_{\text{H}}^2 & \text{for } n \ll n_{\text{crit}} \\ \Lambda^{(\text{LTE})} \propto n_{\text{H}} & \text{for } n \gg n_{\text{crit}} \end{cases} \quad (9)$$

The critical density n_{crit} , above which de-excitation due to collisions dominates over the competing radiative decay, is a function of temperature only, and is defined as

$$n_{\text{crit}} \equiv \frac{\Lambda^{(\text{LTE})}}{\Lambda^{(n \rightarrow 0)}} n_{\text{H}} \quad . \quad (10)$$

The cooling function can finally be expressed in the form

$$\Lambda = \frac{\Lambda^{(\text{LTE})}}{1 + n_{\text{crit}}/n_{\text{H}}} \quad , \quad (11)$$

smoothly joining the low-density with the high-density case. In Figure 2, we show this cooling function for various densities. At a given temperature, the cooling per molecule (Λ/n_{H_2}) first increases with density, but then approaches (for $n > n_{\text{crit}}$) the LTE value which constitutes the maximum possible cooling rate. Since H_2 has a comparatively small moment of inertia, $I \simeq m_{\text{H}} a_0^2$, the rotational energy, $E_{\text{rot}} = L^2/2I$, is correspondingly large for a given amount of angular momentum $L = \hbar \sqrt{J(J+1)}$. Estimating the internuclear separation to be of order the

Bohr radius, $a_0 \simeq 0.5 \text{ \AA}$, one then finds for the lowest-lying ($2 \rightarrow 0$) rotational transition the equivalent minimum temperature

$$T_{\text{min}} = \frac{\Delta E_{20}}{k_B} = \frac{6\hbar^2}{2m_{\text{H}} a_0^2 k_B} \quad , \quad (12)$$

resulting in $T_{\text{min}} \sim 500$ K. The high-energy tail of the Maxwellian velocity distribution will allow the gas to attain somewhat lower temperatures, but it is one of the crucial aspects of the primordial gas physics that cooling down to temperatures below $T \sim 100$ K is not possible in the absence of coolants other than molecular hydrogen. The corresponding critical density for $T \sim 100 - 300$ K is then $n_{\text{crit}} \simeq 10^3 - 10^4 \text{ cm}^{-3}$. These characteristic values of temperature and density, based on the microphysics of H_2 cooling, leave their imprint on the thermal evolution of the primordial gas, as will be discussed below.

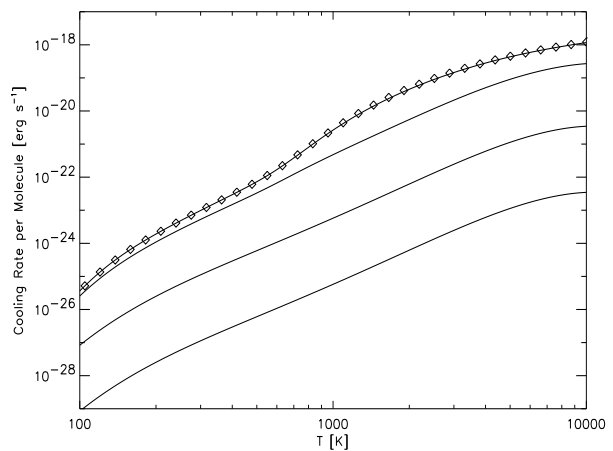


FIG. 2.— H_2 cooling function (Galli & Palla 1998). *Solid lines:* Cooling rates per H_2 molecule for various densities. *From bottom to top:* $n = 10^{-1}, 10^1, 10^3, 10^5 \text{ cm}^{-3}$. *Diamond-shaped symbols:* Cooling rate in LTE. This latter rate gives the maximum possible cooling per molecule at a given temperature. Notice the saturation in the cooling rate due to the transition from NLTE to LTE level populations.

Another possible coolant in the primordial gas is HD, deuterium hydride. The low abundance, $n_{\text{D}} \simeq 10^{-5} n_{\text{H}}$, is partially offset by the fact that HD does possess a permanent electric dipole moment with the correspondingly larger radiative transition probabilities ($A \sim 10^{-8} \text{ s}^{-1}$ for the lowest-lying rotational level, a factor ~ 1000 enhancement over H_2). In addition, since the rotational transition $1 \rightarrow 0$ is allowed, HD cooling can reach lower temperatures than H_2 : $T_{\text{min}} \simeq \Delta E_{10}/k_B \simeq 160$ K. Consequently, cooling due to HD might become important at temperatures $\sim 100 - 200$ K. Our treatment of HD cooling relies on recent work of Flower et al. (2000), who have carefully computed the relevant collisional rates, and provide an analytical fit to their results.

Since radiative cooling to temperatures below that of the CMB

$$T_{\text{CMB}} = 2.7\text{K}(1+z) \quad (13)$$

is thermodynamically not possible, we write for the cooling due to H_2 and HD:

$$\Lambda = \Lambda(T) - \Lambda(T_{\text{CMB}}) \quad (14)$$

This approximate treatment ensures that $T \geq T_{\text{CMB}}$, unless cooling proceeds via adiabatic expansion.

Finally, we have included two cooling mechanisms of lesser importance. Firstly, for temperatures approaching $\sim 10^4$ K, cooling due to collisionally excited lines of atomic hydrogen becomes effective (Cen 1992):

$$\Lambda_{\text{H}} = 7.5 \times 10^{-19} (1 + T_5^{1/2})^{-1} \exp(-118,348/T) n_e n_{\text{[H]}} \quad (15)$$

Only a small fraction of the gas in a Population III DM halo, however, reaches that high a temperature, and atomic hydrogen could not have facilitated the collapse and fragmentation of the primordial gas. Secondly, as long as there remains a residual degree of ionization, energy is exchanged between the photons of the CMB and the electrons of the gas by (normal and inverse) Compton scattering:

$$\Lambda_{\text{Comp}} = 5.4 \times 10^{-36} (1+z)^4 n_e (T - T_{\text{CMB}}) \quad (16)$$

At redshifts below $z \sim 200$, this coupling becomes increasingly weak, and does not significantly contribute to the cooling of the gas.

In Figure 3, we show the relative importance of the various heating and cooling processes for a fluid element, whose time evolution is representative of what we find in our simulations. At early times, while the cloud is still expanding, cooling due to adiabatic expansion dominates. After turnaround, the gas heats up by adiabatic compression. Only close to the moment of virialization does H_2 cooling exceed the adiabatic heating, allowing the gas to cool upon further contraction. In these early stages, cooling due to HD is never important. After virialization, when the gas has settled into a cold (a few 100 K) central configuration, HD cooling becomes somewhat more important, without ever changing the thermal evolution dramatically.

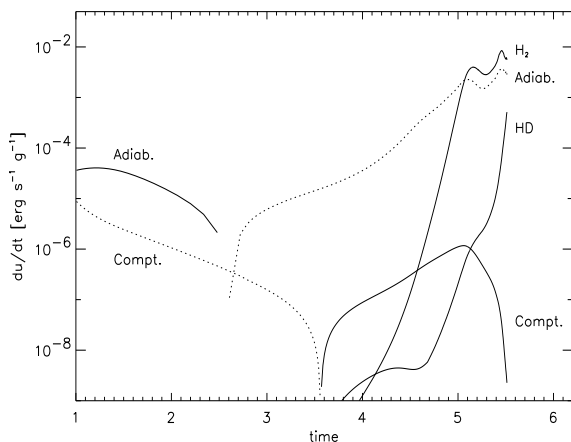


FIG. 3.— Importance of cooling and heating terms during collapse. *Solid lines*: Cooling (in $\text{erg s}^{-1} \text{g}^{-1}$) vs. time. *Dotted lines*: Heating (in $\text{erg s}^{-1} \text{g}^{-1}$) vs. time. Time is measured in units of the initial free-fall time, $\sim 2 \times 10^7$ yr. Adiabatic cooling changes into adiabatic heating after turnaround. Compton heating (for $T < T_{\text{CMB}}$), on the other hand, turns into Compton cooling (for $T > T_{\text{CMB}}$). H_2 is the dominant coolant, but can compete with the heating due to adiabatic compression only close to the moment of virialization.

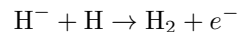
The treatment of radiative cooling, therefore, necessitates knowing the abundances of H_2 and HD. This is the

subject we take up next.

2.2.2. Chemistry

As shown in the previous section, radiative cooling is mainly due to H_2 . Cooling due to HD is less important, but we have included it for the sake of completeness. It is consequently essential to predict the respective abundances of these molecules. The appropriate primordial chemistry has the following simplifying features. Helium is assumed to be always completely neutral, and we neglect all reactions involving He, He^+ , He^{++} . This assumption is justified since the temperature is typically low enough ($T < 10^4$ K) to render the He chemistry inert. In addition, we also ignore all processes of photoionization and -destruction. Although photoreactions due to the CMB are very important at redshifts $z > 100$, they can be safely neglected in our simulations. Finally, there does not yet exist a UV background, prior to the onset of Population III star formation. Since H_2 and HD are formed in nonequilibrium, it is necessary to consider the respective reaction networks. First, we discuss the chemistry of H_2 formation and destruction.

Our H_2 network is based on the compilation of Haiman et al. (1996), and is presented in Table 1. In the absence of dust grains, the main route for the production of H_2 is given by the H^- channel (McDowell 1961):



An alternative formation channel relies on the intermediary H_2^+ . Since the H^- channel always dominates in our simulations, we ignore reactions involving H_2^+ . The validity of this assumption has been tested by comparison calculations with the full network. At redshifts $z > 100$, on the other hand, the H_2^+ channel becomes important due to the ready destruction of H^- , which has a binding energy of only 0.75 eV, by energetic CMB photons. Thus, hydrogen molecules are produced as long as there is a sufficient abundance of free electrons which act as catalysts in the H^- channel. For the low temperatures and weak shocks in the typical collapse of a primordial cloud, there is no efficient way to ionize the gas. The residual abundance of free electrons $x = n_e/n \sim 10^{-4}$ recombines on a timescale $t_{\text{rec}} \simeq (k_{\text{rec}} x n)^{-1} \simeq 10^6 - 10^7$ yr. The recombination coefficient $k_{\text{rec}} \sim 10^{-12} \text{cm}^3 \text{s}^{-1}$ is evaluated for typical temperatures, $T \sim 5000$ K, and densities, $n \sim 10^2 \text{cm}^{-3}$, as found in our simulations. One can then estimate the maximal abundance of hydrogen molecules, $f = n_{\text{H}_2}/n$, according to

$$\frac{f}{t_{\text{rec}}} \sim \frac{df}{dt} \simeq nk_3 x.$$

The rate for the radiative attachment of H^- and e^- (see reaction (3) in Table 1) is approximately $k_3 \sim 10^{-15} \text{cm}^3 \text{s}^{-1}$. The asymptotic abundance of H_2 , produced through the H^- channel, is then $f \simeq k_3 x n t_{\text{rec}} \simeq 10^{-3}$. This prediction is borne out in our simulations under a wide range of circumstances. H_2 abundances of $10^{-4} - 10^{-3}$, albeit low, nevertheless allow the primordial gas to efficiently cool,

thus enabling the condensation into high density structures. Once the gas reaches densities $n > 10^8 \text{ cm}^{-3}$, three-body reactions (Palla et al. 1983) convert the gas rapidly into fully molecular form. These reactions are included in Paper II, where we investigate the further collapse of a high density clump, but are not important here.

The chemistry responsible for the formation and destruction of HD has recently been discussed by Galli & Palla (1998). We adopt their minimum model, as listed in Table 2.

2.3. Properties of the Star Forming Region

To determine the properties of the primordial star forming region, two ingredients have to be considered. Firstly, one needs to know how the dark matter evolves. This history of hierarchical gravitational clustering, resulting in the collapse of increasingly massive DM halos, is specified by the adopted variant of the CDM model. Secondly, one has to address the question of whether the baryons are able to fall together with the dark matter. The opposing effect of gas pressure in collapsing DM halos has been studied by Tegmark et al. (1997). These authors argue that the primordial gas can only undergo continued collapse and fragmentation, and consequently star formation, if it manages to efficiently radiate away the gravitational binding energy which is released in this process. The efficiency of cooling can be quantified by the cooling timescale, $t_{cool} \simeq nk_B T / \Lambda$, and is to be compared with the freefall time, $t_{ff} \simeq 1 / \sqrt{G\rho}$. One then has the classical Rees-Ostriker criterion for fragmentation and continued collapse (Rees & Ostriker 1977): $t_{cool} < t_{ff}$. In the early stages of the collapse, temperatures are low enough ($\sim 1000 \text{ K}$) for cooling to proceed mainly via the lowest-lying rotational transition of H_2 . In evaluating the criterion $t_{cool} < t_{ff}$, Tegmark et al. (1997) find the minimum virial temperature necessary for sufficient cooling, and by applying equ. (4) the corresponding minimum halo mass as a function of collapse redshift. The result of this calculation is that a 3σ -peak of mass $\sim 10^6 M_\odot$, and collapsing at a redshift $z_{vir} \sim 30$, does meet the requirement for efficient cooling. Halos with these characteristic masses and collapse redshifts are therefore predicted to be the sites for the formation of the first stars.

To understand the complicated physics of gas fragmentation, we now turn to a description of our numerical simulations.

3. NUMERICAL METHODOLOGY

In this section, we describe the elements of our numerical approach. The evolution of the dark matter and gas components is calculated with a version of TREESP (Hernquist & Katz 1989), combining the smoothed particle hydrodynamics (SPH) method with a hierarchical (tree) gravity solver. The details of the gravitational N-body solver and the treatment of the hydrodynamics are discussed in the Appendix. We here present our additions to the code which are necessary for the investigation of the primordial gas. These are a method to solve the primordial chemistry network, and a technique to create sink particles.

3.1. Solving the Reaction Network

Following the abundance evolution of the 8 species H , H^+ , H^- , H_2 , D , D^+ , HD , and e^- , entails solving the corresponding coupled set of kinetic equations. Due to the very short reaction timescales, compared to the dynamical time, the adopted method of solution has to be implicit, as in the case of the thermal energy equation. Traditional matrix-based techniques such as the STIFBS routine (Press et al. 1992), or the Livermore LSODAR solver (Hindmarsh 1983), prove to be computationally too expensive for three-dimensional applications. We therefore have implemented a fast method of solution which is based on the approximate backwards differencing formula (BDF). This approach has been pioneered by Anninos et al. (1997). Consider the rate equation for a given species i , which can be expressed as

$$\frac{dn_i}{dt} = -Dn_i + C \quad . \quad (17)$$

All reactions contributing to the destruction of species i are contained in D , while all reactions leading to the production of that species are summarized by the symbol C . Both D and C are functions of temperature and the abundances of the other species. Evaluating the right-hand side of equation (17) at the new timestep, results in the discretization

$$n_i^{new} = \frac{C^{new} \Delta t + n_i^{old}}{1 + D^{new} \Delta t} \quad . \quad (18)$$

We update the hydrogen and deuterium species in the following order, which has been found by experimentation to be both stable and accurate: e^- , H^+ , H^- , H_2 , H , D^+ , HD , D . An estimate for C^{new} and D^{new} is obtained by first inserting the abundances at the old timestep, and then successively replacing them with the updated ones, as the algorithm proceeds from species to species. In determining the abundances of the normal hydrogen species, we do not include the reactions of the deuterium network. This is justified by the very low abundance of deuterium ($n_D \sim 10^{-5} n_H$). The evolution of the deuterium network, on the other hand, crucially depends on the abundances of the normal hydrogen species.

For increased accuracy, a subcycling procedure is adopted: The algorithm loops over the species repeatedly, each time with a small timestep Δt_{sub} given by

$$\Delta t_{sub} = \epsilon \frac{n_e}{\dot{n}_e} \quad , \quad (19)$$

where n_e is the abundance of free electrons, and $\epsilon = 0.1$ is an accuracy parameter.

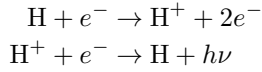
The reactions determining the abundance of the intermediary species H^- proceed much more rapidly than the other reactions. Therefore, one can safely assume that H^- is always present with its equilibrium value:

$$n_{\text{H}^-} = \frac{k_3 n_{\text{H}} n_e + k_6 n_{\text{H}_2}}{(k_4 + k_{11}) n_{\text{H}} + (k_5 + k_{12}) n_{\text{H}^+} + k_{10} n_e} \quad . \quad (20)$$

The identification of the reaction rates can be found in Table 1.

To test our chemistry solver, we compare the analytically determined equilibrium abundances as a function of temperature, obtained by setting $dn_i/dt = 0$ for all i , with

those given by the chemistry solver, after the integration has converged. The analytical estimates are derived as follows. For H^+ , we assume $n_e = n_{\text{H}^+}$ and consider the collisional balance:



With the reaction rates in Table 1, one finds

$$n_{\text{H}^+} = \frac{k_1}{k_2} n_{\text{H}} \quad . \quad (21)$$

The abundance of atomic hydrogen is assumed to be $n_{\text{H}} = n_{\text{H},\text{tot}} - n_{\text{H}^+}$, where $n_{\text{H},\text{tot}}$ is the total density of normal hydrogen. For H_2 , we obtain (see Table 1):

$$n_{\text{H}_2} = \frac{k_4 n_{\text{H}} n_{\text{H}^-}}{(k_6 + k_8 + k_9) n_{\text{H}} + k_7 n_{\text{H}}} \quad . \quad (22)$$

The abundance of the intermediary species H^- is given by equation (20), evaluated with $n_{\text{H}_2} = 0$. For the deuterium species, D^+ and HD , the corresponding expressions are:

$$n_{\text{D}^+} = \frac{k_{D2} n_{\text{D}} n_{\text{H}^+}}{k_{D1} n_e + k_{D3} n_{\text{H}}} \quad , \quad (23)$$

and

$$n_{\text{HD}} = \frac{k_{D4} n_{\text{D}^+} n_{\text{H}_2}}{k_{D5} n_{\text{H}^+}} \quad . \quad (24)$$

Here, k_{D1}, k_{D2}, \dots correspond to the reactions in Table 2, and we assume $n_{\text{D}} = n_{\text{D},\text{tot}} - n_{\text{D}^+}$, with $n_{\text{D},\text{tot}}$ being the total density of heavy hydrogen. The result of this comparison is presented in Figure 4. As can be seen, the chemistry solver nicely reproduces the analytical expectation.

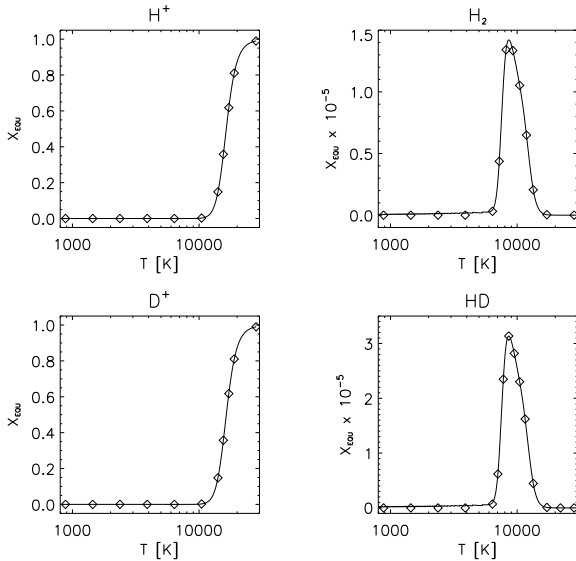


FIG. 4.— Testing the chemistry solver. Shown are the equilibrium abundances for the species H^+ , H_2 , D^+ , and HD . In each case, fractional abundance is plotted vs. temperature. *Solid lines*: Abundances from allowing the chemistry solver to reach convergence (to within 10^{-10}). *Diamond-shaped symbols*: Analytic estimate for the equilibrium value. It can be seen that the equilibrium abundances are nicely reproduced by the solver. Notice also the extreme similarity between the normal hydrogen and the deuterium species.

3.2. Creation of Sink Particles

When in the course of a simulation the gas attains increasingly high density, the SPH smoothing length decreases according to $h \simeq N_{\text{neigh}}^{1/3} n^{-1/3}$. The Courant condition then enforces the adoption of smaller and smaller timesteps $\Delta t \simeq h/c_s$, with c_s being the sound speed. Upon the onset of gravitational instability and the resulting runaway collapse, the simulation therefore effectively grinds to a halt. To overcome this fundamental numerical limitation, and to be able to follow the evolution of the overall system for a few dynamical times, a method of creating sink particles is necessary. Here, we describe our strategy in doing so. Recently, Bate, Bonnell, and Price (1995) have developed another such technique in the context of SPH and applied it to the study of protobinary accretion.

In developing the algorithm, one has to address the following questions. (1) *When a sink particle is created during a simulation, would the incorporated particles really continue to collapse, or would they escape again from each other, if one were to follow their evolution further?* To ensure that only gravitationally bound particles are merged to form a sink particle, we utilize the runaway nature of the Jeans instability. Consider how the density does evolve with time for the SPH particles close to the first collapsing region. Densities are initially close to $n \sim 10^4 - 10^5 \text{ cm}^{-3}$, and subsequently either experience only a modest rise in density, or a rapid increase by many orders of magnitude. This dichotomy allows for the unambiguous identification of the collapsing gas particles. The first, and physically most important, criterion for a particle to be eligible for merging therefore is: (a) $n > n_{\text{th}}$. The value of n_{th} has to be adjusted to the physical characteristics of the problem. We find that $n_{\text{th}} = 10^8 \text{ cm}^{-3}$ works well in our case of primordial gas which collapses and fragments in the center of a dark matter halo. Another reason for this choice lies in the fact that beyond a density of 10^8 cm^{-3} , additional physics has to be considered: Three-body reactions convert the gas into fully molecular form, and opacity effects start to become important. We address this high-density regime in Paper II, but otherwise assume that $n < 10^8 \text{ cm}^{-3}$. A second test a particle has to pass is: (b) $\nabla \cdot \vec{v} < 0$, i.e., that it is part of a converging flow.

To further examine whether a given collection of particles is gravitationally bound, one has to determine whether the binding energy of the system is negative (criterion (c)):

$$E_{\text{total}} = E_{\text{grav}} + E_{\text{kin}} + E_{\text{th}} < 0 \quad , \quad (25)$$

where E_{grav} , E_{kin} , and E_{th} are the total gravitational, kinetic, and thermal energies, respectively. A system will continue to collapse only if gravity overwhelms the combined opposing efforts of thermal pressure and rotation. Defining the usual parameters $\alpha = E_{\text{th}}/|E_{\text{grav}}|$ and $\beta = E_{\text{rot}}/|E_{\text{grav}}|$, with E_{rot} being the total rotational energy of the system, the requirement of continued collapse can be written as (criterion (d)):

$$\alpha + \beta < 1 \quad . \quad (26)$$

In Figure 5, we show these quantities as a function of distance from the density maximum, at the instant of creating the sink particle.

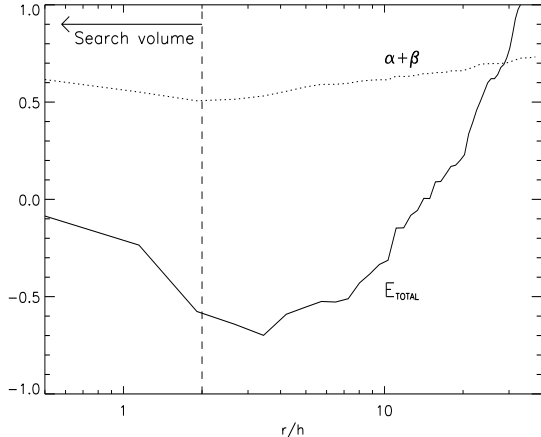


FIG. 5.— Search radius for inclusion into sink particle. *Solid line*: Total energy vs. distance from density maximum. The total energy of all particles within a given radius is defined as $E_{total} = E_{grav} + E_{kin} + E_{th}$, and plotted with an arbitrary normalization. Distances are in units of $h(r_{max})$, the smoothing length of the particle with the highest density. *Dotted line*: Sum of the ratios $\alpha = E_{th}/|E_{grav}|$ and $\beta = E_{rot}/|E_{grav}|$ vs. r/h . Only particles within $\Delta r < 2h$ (*dashed line*) are considered to become part of the sink particle. It is evident that this is a very conservative choice, safely meeting the criteria $\alpha + \beta < 1$ and $E_{total} < 0$. A more aggressive merging would search within $\Delta r < 10h$, but this would entail a more elaborate testing of whether a candidate particle would really end up in the clump, or escape again.

Our merging algorithm now proceeds by sorting the eligible particles according to density. Subsequently, a search is performed within a range of $r_{search} = 2h_{max}$ around the particle with the highest density. All particles within this volume are merged to form the sink particle, provided they fulfill criteria (a) and (b). This procedure is repeated until all eligible particles are assigned to a sink particle. We assume that passing criteria (a) and (b) implies $E_{total} < 0$ and $\alpha + \beta < 1$, without explicitly testing for it. This assumption is justified by the following physical argument. As can be seen in Figure 5, the choice of $r_{search} = 2h_{max}$ is very conservative. All particles within this search volume are safely bound, and far from pressure or rotational support. Surrounding the search volume, there is a massive, collapsing envelope which is part of the Jeans unstable flow. Consequently, a more aggressive merging could be adopted with $r_{search} \simeq 10h_{max}$. To reliably determine whether one of the less bound, outer particles is to be merged, the explicit testing for criteria (c) and (d) would be necessary in this case (Bate et al. 1995). We have carefully verified the reliability of our merging procedure by performing test calculations with and without criteria (c) and (d), and find that in each case our assumption, (a)+(b) \Rightarrow (c)+(d), is valid.

The next conceptual step concerns the properties of the newly created sink particle, and how to treat the boundary to the neighboring region. This leads to the second question: (2) *Does the presence of a sink particle unphysically affect the SPH particles in its vicinity?* Upon its formation, the sink particle (or clump) has mass

$$M_{Cl} = \sum_i m_i, \quad (27)$$

a mass-weighted position vector

$$\vec{r}_{Cl} = \frac{\sum_i m_i \vec{r}_i}{M_{Cl}}, \quad (28)$$

and a mass-weighted velocity

$$\vec{v}_{Cl} = \frac{\sum_i m_i \vec{v}_i}{M_{Cl}}, \quad (29)$$

where the summation extends over all contributing particles. We treat the sink particle as being still gaseous, and as consequently still participating in the SPH interactions and smoothing procedure. A constant gas density, $n_{Cl} = n_{th}$, and temperature, $T_{Cl} = \sum_i m_i T_i / M_{Cl}$, are assigned to the clump. The resulting (constant) pressure is higher than in the surroundings which is slightly less dense and hot. This prescription approximately models a negative pressure gradient. The unphysical infall of neighboring particles onto the clump is therefore prevented. Such a situation would occur if the sink particle were assumed to be collisionless, unless special care is taken to formulate appropriate boundary conditions (see Bate et al. (1995)). With continuing mass accretion, gravity becomes increasingly dominant, and the sink particle asymptotically assumes a fully collisionless character. In Figure 6, we demonstrate that this procedure leads to a satisfactory treatment of the boundary between the clump and its neighboring particles.

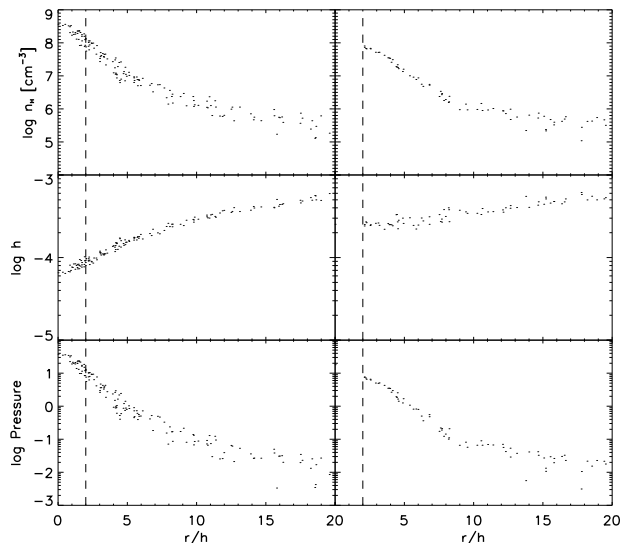


FIG. 6.— Effect of merging on neighboring particles. *Right column*: Properties of SPH particles in the vicinity of the sink particle, briefly after its creation. *Left column*: Particle properties for the comparison case, where no merging takes place, and the gas evolution is followed to increasingly higher density. *Top panels*: Number density vs. distance from density maximum. Distances are in units of $h(r_{max})$, the smoothing length of the particle with the largest density, evaluated at the instant of merging. *Middle panels*: Smoothing length vs. r/h . *Bottom panels*: Gas pressure vs. r/h . The vertical lines at $r/h = 2$ delineate the effective size of the sink particle. It can be seen that the thermodynamic properties, together with the radial gradients of density and pressure, are very similar in the two cases. The smoothing lengths, on the other hand, are noticeably larger in the presence of a sink particle. This is to be expected, since removal of particles entails a degrading spatial resolution.

The final element of the algorithm handles the subsequent accretion of gas, and addresses the question: (3) *Is the accretion of a given gas particle physically justified, or does the particle venture only temporarily into the*

vicinity of the clump? A particle is accreted onto a pre-existing clump if criteria (a) and (b) are fulfilled, and if it approaches to within the accretion radius $r_A = 2h_{Cl}$, where h_{Cl} is the smoothing length of the accreting clump. This procedure proves to be very reliable, again due to the fact that in order to reach a density of 10^8 cm^{-3} , the particle has to be part of a Jeans unstable gas flow which has already proceeded well into its runaway collapse. The position and velocity of the merged clump and accreted particle are again taken to be the mass-weighted averages. The density and temperature of the clump retain their initial values, as mentioned above.

This algorithm allows us to investigate the complex dynamics of clump formation, subsequent gas accretion, and the occasional merger of clumps.

4. THE SIMULATIONS

With all the ingredients in hand, we now turn to the description of our simulations, and present an exploratory survey of how the primordial gas behaves under a wide range of initial conditions. We begin by describing our procedure of initializing the numerical simulations, and explaining our choice of parameters. We then turn to the description of the simulations, focusing first on the early evolutionary stages, and subsequently on the later ones.

4.1. Initial Conditions

We model the site of primordial star formation as an isolated overdensity, corresponding to a high- σ peak in the random field of density perturbations. The numerical simulations are initialized at $z_i = 100$ by endowing a spherical region, containing dark matter and gas, with a uniform density and a Hubble expansion according to the top-hat solution (see Section 2.1). The top-hat overdensity is embedded in an Einstein-deSitter universe with a Hubble constant $h = H_0/(100 \text{ km/s/Mpc}) = 0.5$. We consider halos collapsing at $z_{vir} \simeq 20$ and at $z_{vir} \simeq 30$, corresponding to $\sim 2\sigma$ and $\sim 3\sigma$ peaks, respectively, with total masses of $2 \times 10^5 M_\odot$ and $2 \times 10^6 M_\odot$. The baryonic mass fraction is usually taken to be $\Omega_B = 0.05$, but we also consider the case $\Omega_B = 0.20$.

While this is clearly a rather idealized initial configuration, the subsequent evolution of the halo quickly departs from a simple, monolithic collapse. In response to the imprinted small-scale DM fluctuations (see below), the halo develops a very lumpy, nonspherical morphology. This model, which allows for the formation of DM substructure, and the hierarchical merger of DM clumps, embedded in a collapsing background medium, does qualitatively describe the dynamical behavior of the cold dark matter on very small scales.

The major shortcoming of this approach lies in the inability to self-consistently incorporate the angular momentum of the halo. In a realistic cosmological setting, angular momentum is generated by the tidal interaction of neighboring overdensities which are, in general, nonspherical. For an isolated halo, one therefore has to specify the distribution and magnitude of the angular momentum in an explicit way. We here assume that the halo is initially in rigid rotation with a given angular velocity ω . We prescribe ω in accordance with the prediction for the spin parameter λ , as found in cosmological N-body simulations (see Section 2.1). In computational units with $G = M = R = 1$,

one approximately has the relation: $\omega \simeq 6.7\lambda$. The initial angular velocity has values $\omega = 0.1, 0.2$, and 0.4 , corresponding to $\lambda = 0.015, 0.03$, and 0.06 , respectively.

We now describe our procedure of initializing the positions and velocities of the DM and gas particles. To imprint small-scale density fluctuations on the dark matter, we carry out the following steps. After setting up the DM particles on a Cartesian grid, we impose periodic boundary conditions, and perturb the particles according to the Zeldovich (1970) approximation. The random density field $\delta(\vec{x})$ has the Fourier decomposition $\delta = \sum \delta_{\vec{k}} \exp(i\vec{k} \cdot \vec{x})$ with $\delta_{\vec{k}} = A_{\vec{k}} \exp(i\varphi_{\vec{k}})$. A given mode with wavevector \vec{k} is specified by the random phase $\varphi_{\vec{k}}$, distributed uniformly in the interval $[0, 2\pi]$, and the amplitude $A_{\vec{k}} = \nu \sqrt{P(k)}$, where ν is drawn from a Rayleigh distribution (see Padmanabhan 1993). The particles, having undisturbed position \vec{q} , are displaced in such a way as to reproduce the desired density field. In the Zeldovich approach, one finds for the displaced particle position: $\vec{x} = \vec{q} + \vec{f}(\vec{q})$. The displacement field \vec{f} is related to the density via $\delta = -\nabla \cdot \vec{f}$. It is then straightforward to show that $\vec{f} = \sum \vec{f}_{\vec{k}} \exp(i\vec{k} \cdot \vec{q})$ with $\vec{f}_{\vec{k}} = i\delta_{\vec{k}} \vec{k} / k^2$. The Zeldovich approximation also allows one to self-consistently assign peculiar velocities: $\vec{v}_{pec,i} = H_i \vec{f}_i$, where H_i is the Hubble parameter at $z_i = 100$. Adding the peculiar velocity to the Hubble expansion and the solid-body rotation, gives the resulting initial velocity for each DM particle: $\vec{v}_i = \vec{v}_{H,i} + \vec{v}_{rot,i} + \vec{v}_{pec,i}$.

For Gaussian fluctuations, the power spectrum $P(k) = |\delta_{\vec{k}}|^2 = Ak^n$ fully describes the random density field. On small scales ($M < 10^7 M_\odot$), the standard CDM model predicts an asymptotic behavior of $P(k) \propto k^{-3}$, and we take $n = -3$ as our standard value. To investigate the dependence of the gas fragmentation on the character of the DM substructure, we also consider the case $P(k) \propto k^0$, corresponding to white-noise perturbations. To finally fix the amplitude A , we specify the initial variance of the fluctuations

$$\sigma_i^2 = A \sum k^n \quad . \quad (30)$$

The summation is over all contributing modes, where the minimum wavenumber is given by the overall size of the Cartesian box, and k_{max} by the Nyquist frequency. We typically have $\sigma_i^2 \simeq 0.1$.

The rms fluctuation at the moment of collapse is then

$$\sigma(z = 30) = \left(\frac{1 + z_i}{1 + z} \right) \sigma_i \simeq 1 \quad .$$

This choice ensures that the substructure develops on a similar timescale as the overall collapse of the background medium. A potential problem with this initialization procedure is the poor sampling of \mathbf{k} -space for the longest wavelength modes. Since the overall structure of the halo is predominantly determined by these modes (for a k^{-3} spectrum), the DM morphology will change significantly from one random realization to the next, and we can therefore not claim to have simulated the DM morphology in a representative way. This is true in particular for the early stages of the collapse, whereas at later times, different initial configurations approach similar equilibrium states. To

remedy this shortcoming, we have studied cases with different random realizations of the DM fluctuations, keeping all other parameters constant. Finally, all particles within a given radius are selected for the simulation. The typical number of DM particles is $N_{\text{DM}} \simeq 17,000$, but we have also performed test calculations with $N_{\text{DM}} \simeq 130,000$.

The SPH particles, representing the baryonic component, are placed randomly within the given spherical volume. This procedure inevitably introduces unphysical shot-noise. As opposed to the dark matter, however, these numerically induced perturbations are quickly erased by pressure forces, since the initial gas mass is close to the Jeans mass, $M_J \sim 10^5 M_\odot$. The gas particles have velocities, consisting of Hubble expansion and rigid rotation: $\vec{v}_i = \vec{v}_{H,i} + \vec{v}_{rot,i}$. The fractional free electron and hydrogen molecule abundances are taken to be, respectively, $x_i = 4.6 \times 10^{-4}$ and $f_i = 2 \times 10^{-6}$ (Anninos & Norman 1996). We assume a deuterium abundance of $n_{\text{D}} = 4 \times 10^{-5} n_{\text{H}}$ (Galli & Palla 1998), and initialize the density of D^+ and HD according to $n_{\text{D}^+} = 10^{-8} n_{\text{H}}$, and $n_{\text{HD}} = 10^{-3} n_{\text{H}_2}$, respectively. The gas temperature is finally chosen to be $T_i = 200$ K. The typical number of SPH particles is $N_{\text{SPH}} \simeq 16,384$, but we have also performed simulations with $N_{\text{SPH}} \simeq 65,536$ and $N_{\text{SPH}} \simeq 131,072$, to test for convergence.

Initializing our simulations at $z_i = 100$ poses the question whether this is early enough to investigate objects that are collapsing at $z \sim 30$. The crucial initial values for the chemical abundances, the gas temperature and density are actually obtained by integrating the respective governing equations beginning at $z = 1100$, along the line of Tegmark et al. (1997). Although the use of the Zeldovich approximation in advancing the density perturbations to $z_i = 100$ will introduce an error, the overall nature of the DM collapse would not change in a significant way if the simulations were started at somewhat higher redshift.

In Table 3, we summarize the parameters of the different simulations. Run A constitutes the fiducial case, which we will describe first, and against which we subsequently compare the other runs.

4.2. Early Evolution

Given the almost complete absence of observations to constrain the theoretical study of primordial star formation, it is important to single out the essential physical processes. We here present evidence for the existence of characteristic values for the temperature and density of the primordial gas, which in turn translate into a characteristic Jeans scale for fragmentation. To illustrate this characteristic behavior, we first describe a fiducial simulation (Run A) in greater detail, and then investigate the effect of varying the initial conditions.

4.2.1. The Characteristic Mass Scale for Fragmentation

The parameters of Run A, a halo of total mass $2 \times 10^6 M_\odot$ with $10^5 M_\odot$ in baryons, and virializing at $z_{\text{vir}} \simeq 30$, are chosen to safely satisfy the Rees-Ostriker criterion for continued collapse and fragmentation, $t_{\text{cool}} < t_{\text{ff}}$ (see Section 2.3). In a previous publication, we have described a similar case (Bromm, Coppi, & Larson 1999). The simulation presented here has improved on that earlier treatment by including cooling due to HD, and a more realistic initial

H_2 abundance of $f_i = 2 \times 10^{-6}$ (instead of $f_i = 10^{-4}$). Furthermore, Run A is initialized with a different random realization of the DM fluctuation field.

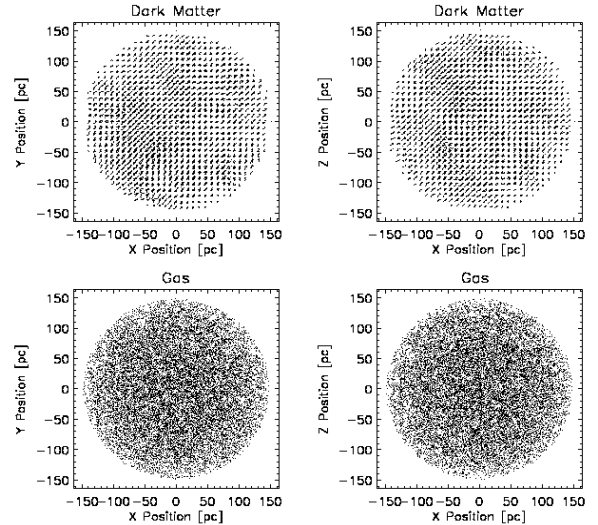


FIG. 7.— Run A: Initial configuration for top-hat collapse. The halo has a total mass of $2 \times 10^6 M_\odot$, and is endowed with a Hubble expansion such that virialization occurs at $z_{\text{vir}} \simeq 30$. *Top row:* The DM particles are perturbed from a regular grid according to $P(k) \propto k^{-3}$. *Bottom row:* The gas particles are placed at random, and comprise a mass fraction of $\Omega_B = 0.05$. Both components are initially in solid body rotation with the angular momentum vector pointing in the z -direction. *Left panels:* Face-on view. *Right panels:* Edge-on view.

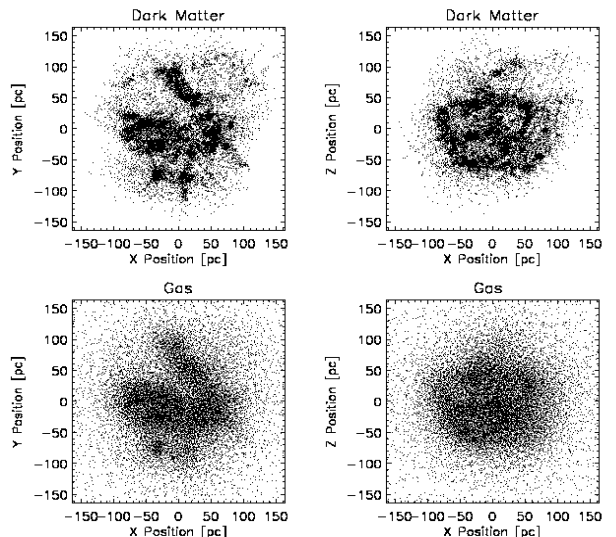


FIG. 8.— Run A: Morphology at $z = 33.5$. The manner of presentation is the same as in Figure 7. The DM has developed significant substructure, and the baryons are just beginning to fall into the corresponding potential wells.

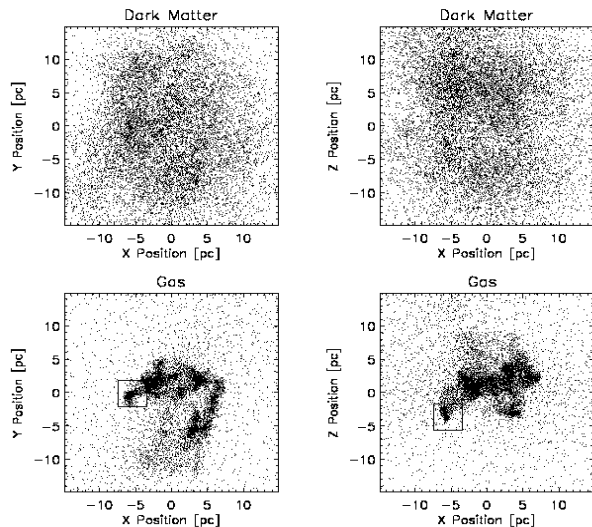


FIG. 9.— Run A: Morphology at $z = 31.2$. The convention in Fig. 7 is adopted for the rows and columns. The box size is 30 pc. The DM is in the process of undergoing violent relaxation with the concurrent smoothing out of the substructure. Having developed a lumpy and elongated morphology, the gas has settled into the center of the DM potential well. Shown is the situation briefly after the formation of the first clump of mass $1400M_{\odot}$ (*small box*).

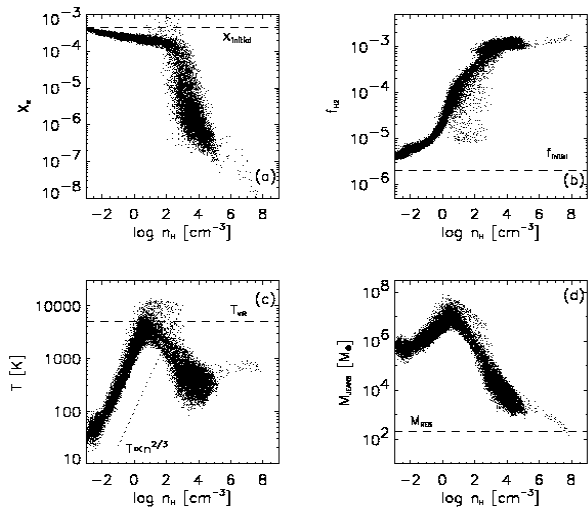


FIG. 10.— Run A: Gas properties at $z = 31.2$. (a) Free electron abundance vs. hydrogen number density (in cm^{-3}). At densities exceeding $n \sim 10^3 \text{ cm}^{-3}$, recombination is very efficient, and the gas becomes almost neutral. (b) Hydrogen molecule abundance vs. number density. After a quick initial rise, the H_2 abundance approaches the asymptotic value of $f \sim 10^{-3}$, due to the operation of the H^- channel. (c) Gas temperature vs. number density. At densities below $\sim 1 \text{ cm}^{-3}$, the gas temperature rises because of adiabatic compression until it reaches the virial value of $T_{\text{vir}} \simeq 5000 \text{ K}$. At higher densities, cooling due to H_2 drives the temperature down again, until the gas settles into a quasi-hydrostatic state at $T \sim 500 \text{ K}$ and $n \sim 10^4 \text{ cm}^{-3}$. Upon further compression due to the onset of the gravitational instability, the temperature experiences a modest rise again. (d) Jeans mass (in M_{\odot}) vs. number density. The Jeans mass reaches a value of $M_J \sim 10^3 M_{\odot}$ for the quasi-hydrostatic gas in the center of the DM potential well, and reaches the resolution limit of the simulation, $M_{\text{res}} \simeq 200 M_{\odot}$, for densities close to the merging threshold of $n = 10^8 \text{ cm}^{-3}$.

In Figure 7, we show the initial configuration of Run A at $z_i = 100$. Comparing the dark matter and gaseous

components, the different way of initializing them, as described above, is clearly visible. Initially, the halo is still expanding, until the moment of turnaround at $z_{\text{ta}} \simeq 50$. The subsequent collapse of the dark matter, occurring on a dynamical timescale of $t_{\text{ff}} \sim 1/\sqrt{G\rho(z=100)} \sim 5 \times 10^7 \text{ yr}$, leads to the eventual establishment of virial equilibrium at $z_{\text{vir}} \sim 30$. Since the initial gas pressure is dynamically unimportant, the baryons freely fall together with the dark matter. Upon compression, the gas temperature rises adiabatically until it reaches the virial value

$$T_{\text{vir}} \simeq \frac{GMm_{\text{H}}}{2k_{\text{B}}R_{\text{vir}}} \sim 5000 \text{ K} \quad , \quad (31)$$

where $R_{\text{vir}} \simeq 100 \text{ pc}$ is the virial radius. At this point, enough H_2 molecules have been formed ($f \sim$ a few 10^{-4}) to provide an efficient cooling mechanism. Consequently, the temperature decreases again with further compression. Figure 8 shows the situation at $z = 33.5$, briefly before the virialization of the dark matter. In response to the initially imprinted k^{-3} -noise, the dark matter has developed a pronounced substructure. Evidently, the collapse proceeds in a very inhomogeneous manner, far from the monolithic, spherically symmetric evolution of the analytic top-hat model. The baryons have just begun to fall into the potential wells which are created by the DM substructure. Thus, the DM imparts a ‘gravitational head-start’ to certain regions of the gas, which subsequently act as the nucleization centers for the formation of high-density clumps.

At the end of the free-fall phase, shown in Figure 9, the gas has developed a very lumpy, filamentary structure in the center of the DM potential. By now, the dark matter has lost the memory of the primordial perturbations, but only after having imprinted its signature on the gas. This almost complete erasure of the DM substructure might be due to insufficient numerical resolution, as has been recently suggested by, e.g., Moore et al. (1999). We have performed a test calculation with eight times as many DM particles ($N_{\text{DM}} \sim 130,000$ instead of 17,000), and find no qualitative change, although a still larger number of particles may be required ($10^6 - 10^7$) to see the survival of the DM lumps.

The corresponding thermodynamic and chemical state of the gas is summarized in Figure 10. Since the abundances, temperature and density are plotted for every SPH particle, this mode of presentation has an additional dimension of information: Particles accumulate (‘pile up’) in those regions of the diagram where the evolutionary timescale is slow. In panel (c) of Figure 10, one can clearly discern such a preferred state at temperatures of a few 100 K, and densities of $10^3 - 10^4 \text{ cm}^{-3}$. These characteristic values have a straightforward physical explanation, along the line of argument presented in Section 2.2 regarding the microphysics of H_2 cooling. A temperature of $T \sim 100 - 200 \text{ K}$ is the minimum one attainable via H_2 cooling. The corresponding critical density, beyond which the H_2 rotational levels are populated according to LTE, is then $n_{\text{crit}} \simeq 10^3 - 10^4 \text{ cm}^{-3}$. Due to the now inefficient cooling, the gas ‘loiters’ and passes through a phase of quasi-hydrostatic, slow contraction.

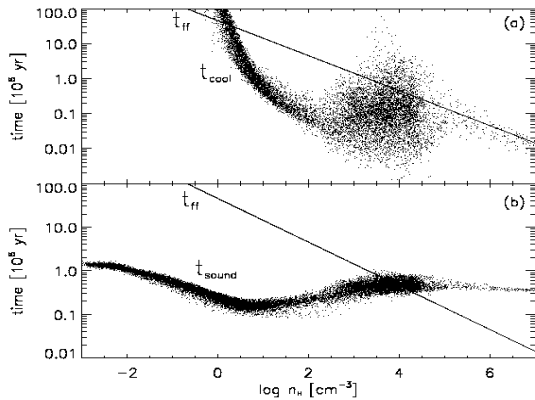


FIG. 11.— Run A: Important timescales at $z = 31.3$. Shown is the situation briefly before the formation of the first clump. **(a)** Free-fall timescale (*solid line*) and cooling timescale (*dotted symbols*) vs. number density (in cm^{-3}). Timescales are in units of 10^6 yr. The gas particles pile up at a density of $n \sim 10^4 \text{ cm}^{-3}$, where $t_{\text{cool}} \simeq t_{\text{ff}}$. **(b)** Free-fall timescale (*solid line*) and sound-crossing timescale (*dotted symbols*) vs. number density (in cm^{-3}). The onset of the Jeans instability (i.e., $t_{\text{sound}} > t_{\text{ff}}$) at $n \sim 10^4 \text{ cm}^{-3}$ coincides with the condition $t_{\text{cool}} \simeq t_{\text{ff}}$ in panel (a).

Further insight can be gained by considering the characteristic timescales of the problem, which are displayed in Figure 11. We consider the free-fall time t_{ff} , the cooling time $t_{\text{cool}} \simeq nk_{\text{B}}T/\Lambda_{\text{H}_2}$, and the sound-crossing time $t_{\text{sound}} \simeq L_{\text{char}}/c_{\text{s}}$. Here, $L_{\text{char}} \simeq 1 \text{ pc}$ is the characteristic size of the filamentary gas in Figure 9. The comparison of t_{cool} and t_{ff} explains the evolutionary behavior of the gas, as described above. At densities exceeding $n \sim 10^0 \text{ cm}^{-3}$, the gas can cool efficiently (i.e., $t_{\text{cool}} < t_{\text{ff}}$), until it reaches the quasi-hydrostatic phase, where $t_{\text{cool}} \sim t_{\text{ff}}$. To move away from this loitering regime, and to attain higher densities, the gas has to become gravitationally unstable. The condition for the onset of instability, $t_{\text{sound}} > t_{\text{ff}}$, is shown in panel (b) of Figure 11. The gas is Jeans unstable for $n > 10^4 \text{ cm}^{-3}$. Alternatively, we can evaluate the Jeans mass for the characteristic values $T \sim 200 \text{ K}$ and $n \sim 10^3 - 10^4 \text{ cm}^{-3}$, resulting in $M_{\text{J}} \sim 10^3 M_{\odot}$. When enough gas has accumulated in a given region to satisfy $M > M_{\text{J}}$, runaway collapse of that fluid region ensues. We find that the gas becomes self-gravitating ($\rho_{\text{B}} > \rho_{\text{DM}}$) coincident with the onset of the Jeans instability. Although the dark matter has played an important role in determining where most of the gas ends up, it henceforth ceases to influence the primordial gas on its further course to stardom.

4.2.2. The Onset of Gravitational Instability

After the onset of instability, the temperature rises again, up to $T \sim 1000 \text{ K}$ at $n \simeq 10^8 \text{ cm}^{-3}$, but not sufficiently to halt the collapse. Once the gas has reached a density of $n_{\text{th}} = 10^8 \text{ cm}^{-3}$, a clump (or sink particle) is formed, and we do not follow the evolution to increasingly higher density. The initial mass of the clump, as shown in Figure 9, is $1400 M_{\odot}$, close to the characteristic Jeans mass of $M_{\text{J}} \sim 10^3 M_{\odot}$.

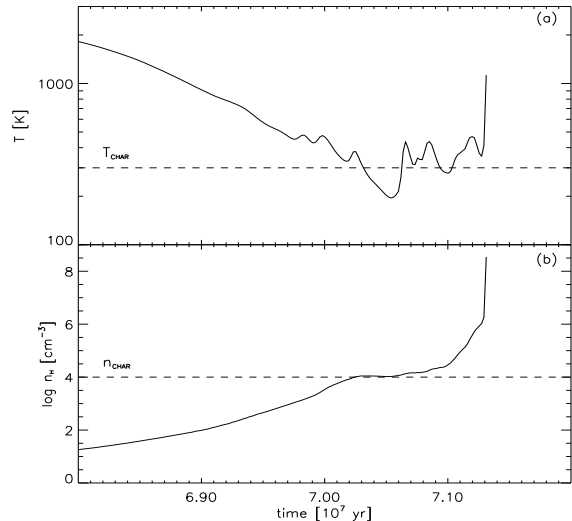


FIG. 12.— History of first runaway fluid element. **(a)** Gas temperature (in K) vs. cosmic time (in 10^7 yr). *Dashed line*: Characteristic temperature $T_{\text{char}} \simeq 300 \text{ K}$. **(b)** Hydrogen number density (in cm^{-3}) vs. cosmic time. *Dashed line*: Characteristic density $n_{\text{char}} \simeq 10^4 \text{ cm}^{-3}$. The fluid element spends $\sim 10^6$ yr at temperatures and densities close to the characteristic values. After this period of “loitering”, the runaway collapse sets in, operating on a timescale $\sim 10^5$ yr.

In Paper II, we take up the question of how the further collapse of a clump does proceed, up to densities of $n \sim 10^{14} \text{ cm}^{-3}$. In doing so, we find no indication for further subfragmentation. Despite the additional boost in the cooling due to the action of three-body reactions, which convert the gas into almost fully molecular form at $n > 10^8 \text{ cm}^{-3}$, no runaway cooling occurs. At the end of the simulation presented in Paper II, a central core of $\sim 100 M_{\odot}$ is in a state of free-fall, surrounded by an extended envelope with an approximately isothermal density profile, $\rho \propto r^{-2}$.

Another way to understand the nature of the runaway collapse is shown in Figure 12, where we plot the history of the first runaway SPH particle. This particle marks the center of the fluid region which is first to become gravitationally unstable. It is evident that the temperature reaches $T \sim 300 \text{ K}$, and subsequently oscillates around that value for approximately 10^6 yr, to finally experience a very rapid rise to $\sim 1000 \text{ K}$. The oscillatory behavior is due to the negative feedback of the H_2 cooling, with increased cooling for higher temperature, and vice versa. Similarly, the density stays at $n \sim 10^4 \text{ cm}^{-3}$ for $\sim 10^6$ yr, before the onset of the runaway collapse.

It has been pointed out by Bate & Burkert (1997) that to avoid numerical fragmentation, one has to resolve the Jeans scale, $M_{\text{J}} > M_{\text{res}}$. One can estimate the resolution limit, M_{res} , of the simulation as

$$M_{\text{res}} \simeq \left(\frac{N_{\text{neigh}}}{N_{\text{SPH}}} \right) M_{\text{B}} \quad . \quad (32)$$

For Run A, where $N_{\text{SPH}} = 16,384$, this results in $M_{\text{res}} \sim 200 M_{\odot}$, and the criterion above is reasonably well satisfied. To test for numerical convergence, we have performed a simulation with $N_{\text{SPH}} = 131,072$ (Run B), and a corresponding mass resolution of $M_{\text{res}} \sim 25 M_{\odot}$. This high-resolution run confirms that clumps initially form with masses close to $\sim 10^3 M_{\odot}$.

It is a longstanding question whether the Jeans mass is relevant for the understanding of the characteristic mass of present-day star formation. In the primordial case, however, where one can argue that magnetic and turbulent pressures are initially unimportant, one is left with the classic battle between gravity and thermal pressure, as originally envisioned by Jeans (1902). Primordial star formation, therefore, might be the most clear-cut setting for the application of the Jeans criterion.

4.2.3. Exploring Parameter Space

We now harness the key advantage of our method, the ability to perform controlled experiments, and ask how sensitive the results, obtained in Run A, are to variations in the initial conditions. Again, we here discuss the simulations up to the formation of the first clumps, and turn to the further clump evolution later.

(i) Spectral index

To investigate the role of the DM substructure, we consider in Run E the case of a white-noise spectrum, $P(k) \propto k^0$. Admittedly, such a spectrum is physically ad hoc, in contrast to the k^{-3} case which is ultimately motivated by the theory of inflation. With the rms fluctuation on a given mass scale being $\sigma(M) \propto M^{-(n+3)/6}$ for spectral index n , one finds

$$\sigma(M) \propto \begin{cases} \text{const.} & \text{for } k^{-3} \\ M^{-1/2} & \text{for } k^0 \end{cases}. \quad (33)$$

The k^{-3} case, therefore, has approximately equal power on all mass scales, whereas the smallest resolvable scale (given by the Nyquist frequency) dominates the white-noise realization.

In Figures 13 and 14, we present the evolution of Run E up to the onset of gravitational instability. This time sequence is to be compared to the corresponding Figures 7 - 9 for Run A. At redshift $z = 33.5$, briefly before virialization, the baryons have not yet begun to fall into the shallow DM potential wells, in contrast to Run A. Towards the end of the free-fall phase, at $z = 31.2$, the gas has settled into a ring-like central configuration with a morphology which is somewhat more regular than in Run A. This distribution derives from the rather homogeneous character of the overall collapse which deviates much less from spherical symmetry than the k^{-3} case. High-density clumps are formed again with initial masses close to $\sim 10^3 M_\odot$, and the full difference to Run A becomes manifest only during the later evolutionary stages, as will be discussed below.

The occurrence of the regular ring structure in Figure 14 might be an artefact of the initial conditions in Run E which are highly symmetric. Such a ring-like configuration, however, is not a typical result. In general, the resulting morphology is a somewhat accidental feature of our results, and is not important for the main conclusions of this study.

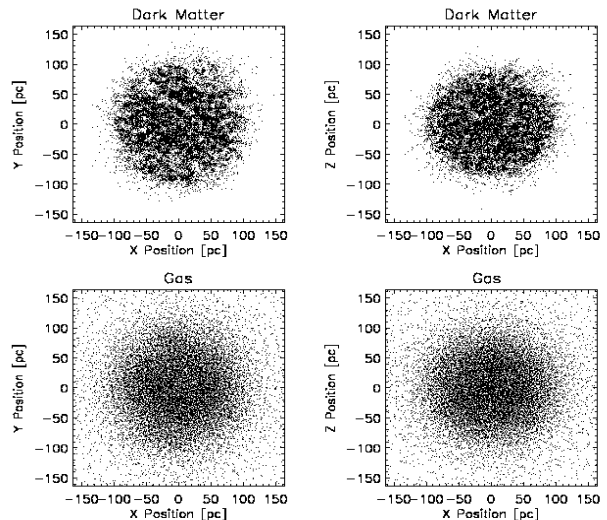


FIG. 13.— Run E: Morphology at $z = 33.5$. The convention in Fig. 7 is adopted for the rows and columns. Compared to Run A in Figure 8, there is relatively more DM substructure on the smallest resolvable scales, and the overall collapse proceeds in a more regular way. The baryons do not yet fall into the shallow DM potential wells.

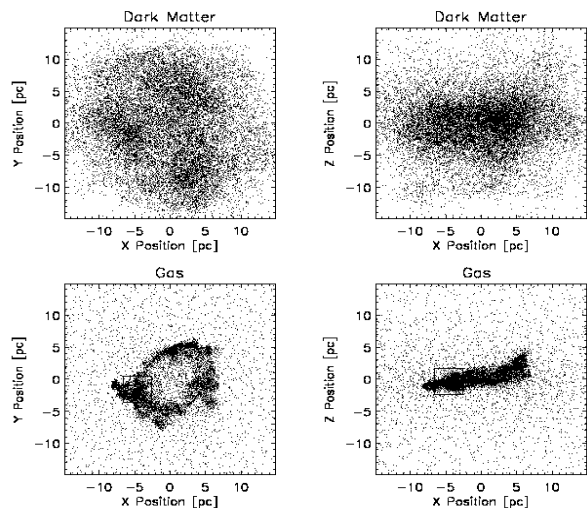


FIG. 14.— Run E: Morphology at $z = 31.2$. The convention in Fig. 7 is adopted for the rows and columns. The boxsize is 30 pc. Shown is the situation briefly before the formation of the first clump (enclosed in the small box). Again, the dark matter is losing its substructure in the process of virialization, whereas the gas has settled into a ring-like, central configuration which has a very knotty appearance.

(ii) Random realization of DM fluctuations

To address the problem of poor k -space sampling for the longest wavelength modes, and the resulting morphological variations in the dark matter, we now compare Runs A and K, and the corresponding Figures 9 and 15. Run K has the same parameters as Run A, but a dark matter component which is perturbed according to a different realization of the Gaussian random process. The appearance of the central gas configuration at $z = 31.2$ is quite different indeed, with a much more extended, filamentary

distribution of gas in Run K. Also, the first two clumps to form have masses close to $\sim 500M_\odot$, compared to the one $\sim 1500M_\odot$ clump in Run A. We will see below, however, that these two cases later on converge to a rather similar state, despite the differences during the early evolutionary stages.

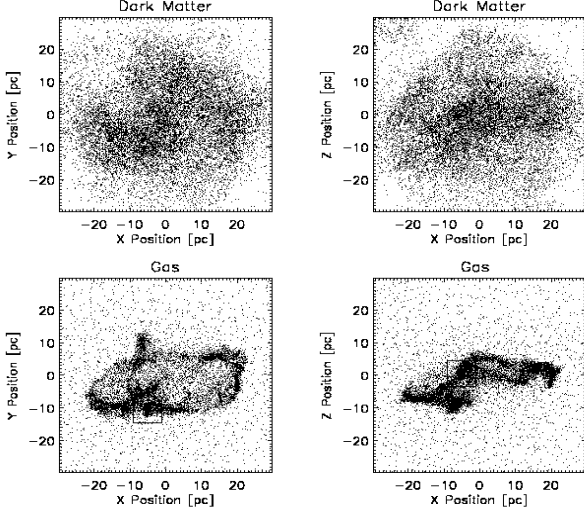


FIG. 15.— Run K: Case with different realization of $P(k) \propto k^{-3}$ noise. Shown is the morphology at $z = 31.2$, briefly after the formation of the first two clumps with masses 360, and $520M_\odot$ (*small box*). The convention in Fig. 7 is adopted for the rows and columns. The boxsize is 60 pc. This case is to be compared to Run A in Figure 9. Both cases have the same initial conditions with the exception of the random realization of the DM fluctuation field. It can be seen that the resulting morphology is very different here, with a much more extended central gas configuration.

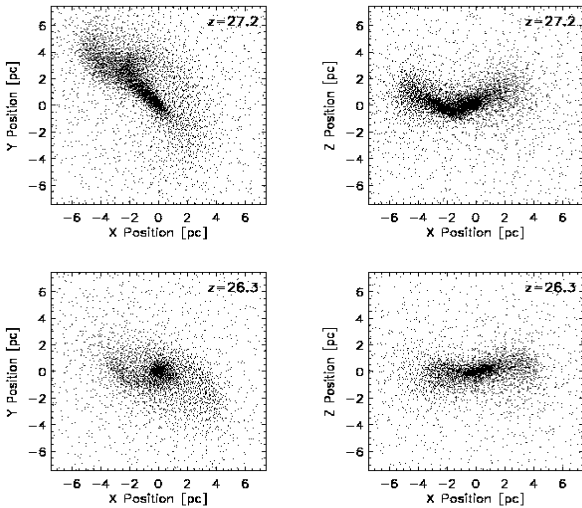


FIG. 16.— Run H: Case of halo with total mass of $2 \times 10^5 M_\odot$. Shown is the morphology of the gas for two subsequent times. *Top row*: Gas distribution at $z = 27.2$, briefly after the formation of a clump with $M \sim 400M_\odot$. *Bottom row*: Gas distribution at $z = 26.3$. By now, the clump has grown in mass to $M \sim 1800M_\odot$. *Left panels*: Face-on view. *Right panels*: Edge-on view. The box has a linear size of 15 pc. In the case of this low-mass halo, where the requirement for efficient cooling, $t_{cool} < t_{ff}$, is only marginally satisfied, one clump forms in the center of the DM potential, and reaches a final mass of $\sim 2000M_\odot$.

(iii) Angular momentum

In Runs C, A, and D with initial angular velocities of $\omega = 0.1, 0.2$, and 0.4 , respectively, we investigate the influence of angular momentum (or spin) on the evolution of the primordial gas. Increasing the amount of spin has two main effects. First, the moment of virialization and of the onset of gravitational instability is delayed, leading to the sequence of collapse redshifts: $z_{vir} \simeq 31.7, 31.2$, and 29.8 for Runs C, A, and D. Second, the gas is less centrally concentrated, resulting in a reduced rate for the merging of clumps, as will be discussed in the following section.

The first effect can be understood in terms of a straightforward modification of the analytical top-hat model, adding to it the presence of angular momentum. By considering the energy balance at turnaround, an estimate for the turnaround radius can be obtained as follows (in dimensionless units where $G = M = R = 1$):

$$\frac{1}{R_{ta}} \simeq 1 - \frac{1}{3}\omega_i^2 - \frac{1}{2}H_i^2, \quad (34)$$

where ω_i and H_i are the initial angular velocity and Hubble parameter, respectively. With the virial radius given by $R_{vir} \simeq 1/2R_{ta}$, the redshift of virialization is approximately

$$1 + z_{vir} \simeq (1 + z_{vir, nr})(1 - 20.5\lambda^2) \quad (35)$$

Choosing the redshift of virialization in the absence of rotation as $z_{vir, nr} = 31.8$, nicely reproduces the numerical results. The presence of angular momentum, therefore, delays the collapse by reducing the binding energy of the halo.

(iv) Halo mass

In Run H, we study the collapse of a less massive halo of total mass $2 \times 10^5 M_\odot$. This case only marginally satisfies the Rees-Ostriker criterion (see Section 2.3). The smaller halo mass translates into a lower virial temperature, $T_{vir} \sim 2000$ K, which in turn leads to a reduced efficiency of H_2 cooling. Consequently, the condition for the termination of the free-fall phase, $t_{cool} \sim t_{ff}$, is reached already at lower densities ($10^2 - 10^3 \text{ cm}^{-3}$). The gas, therefore, goes through a prolonged phase of quasi-hydrostatic contraction, and attains a roughly spherical configuration. In Figure 16, we show the central gas distribution at two successive redshifts. Only one clump forms in the center of the cloud with an initial mass of $\sim 400M_\odot$. Subsequently, this clump grows in mass up to $\sim 2000M_\odot$.

The main difference to Run A, besides the formation of only one clump instead of a few, is that here the Jeans instability proceeds less violent, since the opposing effect of pressure is non-negligible in this case.

(v) Baryon fraction

In a universe with a significant contribution to the critical density in the form of vacuum energy, a larger fraction of the matter resides in the baryonic component. For $\Omega_m = 1 - \Omega_\Lambda = 0.3$, one has $\rho_B \simeq 0.20\rho_m$, where ρ_m is the total density of matter. In Run L, we consider a halo with 20% of the mass in gaseous form. From the outset, this case behaves very different from the simulations with a low baryon fraction. As can be seen in Figure

17, the gravitational instability is already triggered during the free-fall phase in the three dominating DM condensations. Since the thermal properties of the gas are not very different from those in Run A, and there is a four times larger amount of available gas, gravity more easily overwhelms thermal pressure. The peculiar character of Run L continues into the later evolutionary stages, where an altogether larger fraction of the gas is able to condense into high-density clumps.

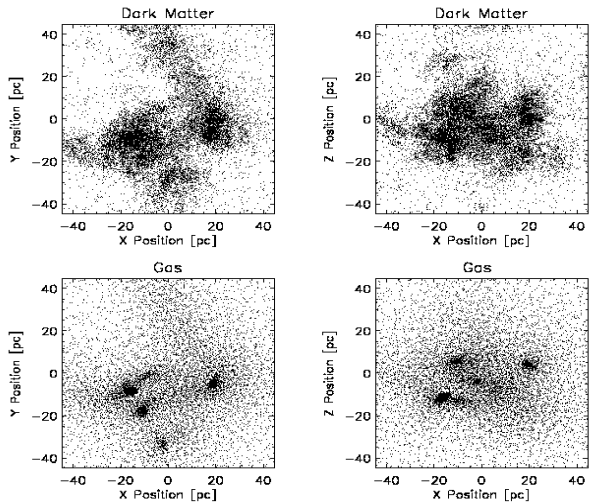


FIG. 17.— Run L: Morphology of case with high Ω_B at $z = 31.7$. The convention in Fig. 7 is adopted for the rows and columns. The boxsize is 90 pc. Shown is the situation briefly after the formation of the first clumps with masses of 750, 850, and $1440M_\odot$. The halo is still in its initial free-fall collapse, and the DM has not yet virialized. Already in this early dynamical stage, the gas in the deepest DM potential wells has undergone runaway collapse. This behavior is in marked contrast to the cases with a low baryon fraction ($\Omega_B = 0.05$).

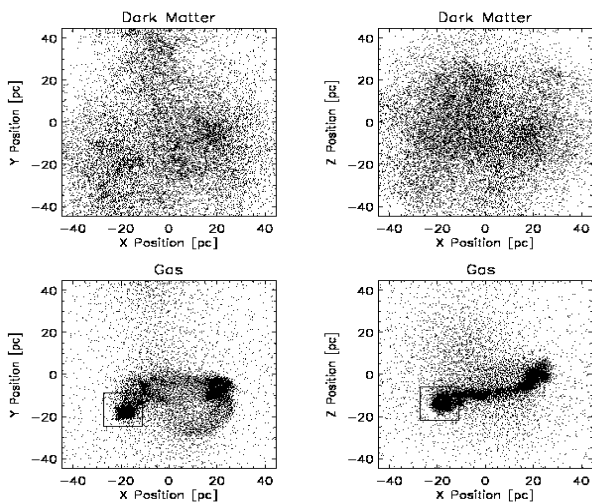


FIG. 18.— Run G: Case of top-hat with $z_{vir} \simeq 20$. Shown is the morphology at $z = 20.6$, briefly after the first clump has formed with a mass of $920M_\odot$ (in the region marked by the small box). The convention in Fig. 7 is adopted for the rows and columns. The boxsize is 90 pc. Compared to Run A (a top-hat of the same mass collapsing at $z_{vir} \simeq 30$) in Figure 9, the resulting gas configuration is much more extended.

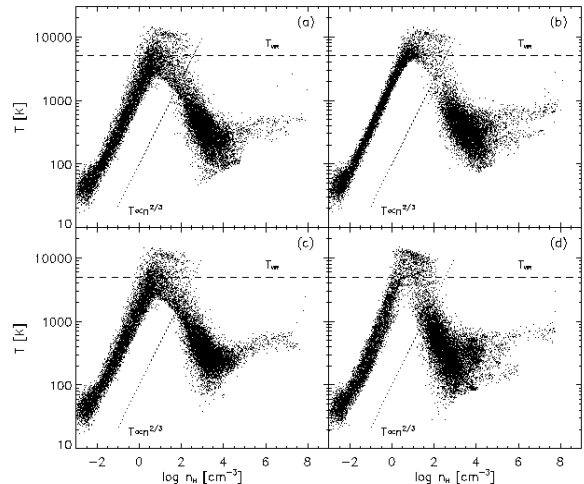


FIG. 19.— Gas properties in simulations with different initial conditions I. Temperature vs. hydrogen number density. All runs are shown at very nearly the same instant, at $z = 31.0$. (a) Fiducial case (Run A): Halo of total mass $2 \times 10^6 M_\odot$, collapsing at $z_{vir} = 30$, initialized with $P(k) \propto k^{-3}$, and including HD cooling. (b) Varying the power spectrum (Run E): Same as (a), but $P(k) \propto k^0$. (c) Varying the cooling (Run F): Same as (a), but no HD cooling. (d) Same as (a), but different realization of the random density field (Run K).

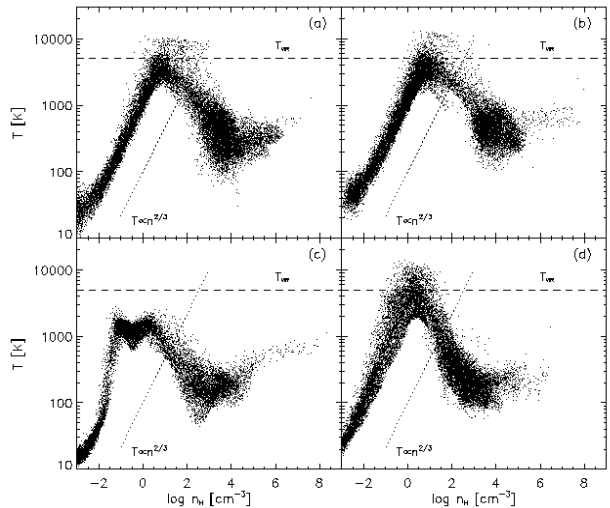


FIG. 20.— Gas properties in simulations with different initial conditions II. Temperature vs. hydrogen number density. (a) Varying the number of particles (Run B): Simulation with large number of SPH particles, shown at $z = 31.0$. For clarity and ease of comparison, only every eighth particle is plotted. (b) Varying the angular momentum (Run C): Low-spin case, shown at $z = 31.7$. (c) Varying the halo mass (Run H): Less-massive halo, shown at $z = 27.2$. (d) Varying the collapse redshift (Run G): Halo with $z_{vir} \simeq 20$, shown at $z = 20.6$. The thermodynamic behavior, displayed in Figures 23 and 24, is very robust under variation of the initial conditions, and in each case, the gas attains characteristic values of temperature and density close to $T \sim 200$ K and $n \sim 10^3 - 10^4$ cm^{-3} , respectively.

(vi) Collapse redshift

In Run G, we consider the collapse of a halo with total mass $2 \times 10^6 M_\odot$, collapsing at $z_{vir} \simeq 20$. Run A and

G correspond to a $\sim 3\sigma$ and $\sim 2\sigma$ peak in the Gaussian random field, respectively. We show the situation briefly after the formation of the first clump in Figure 18, which should be compared to the equivalent stage for Run A in Figure 9. The initial clump mass is again $\sim 10^3 M_\odot$, and the main difference between the two cases lies in the much more extended morphology of the gas in Run G, with a linear size of ~ 40 pc compared to ~ 10 pc in Run A. The larger extension of the central gas configuration is simply due to the smaller binding energy of the halo in Run G, with almost the same amount of initial rotational energy as in Run A. Otherwise, the evolution of the two simulations is very similar.

Summarizing the results from our exploratory survey up to the onset of gravitational instability, two important lessons can be learned. First, the morphology of the collapse varies significantly among the different cases, depending on the initial conditions. Second, the thermodynamic behavior of the primordial gas is very similar for all the cases studied, despite the morphological diversity. To demonstrate this, we show in Figures 19 and 20 the location of the individual SPH particles in the temperature vs. density plane for eight different runs. As can be seen, in each case, the gas does attain the characteristic values of the temperature and density, $T \sim$ a few 100 K and $n \sim 10^3 - 10^4 \text{ cm}^{-3}$. In this preferred region of $T - n$ space, the evolution of the system slows down, allowing to imprint the corresponding characteristic Jeans scale of $M_J \sim 10^3 M_\odot$ onto the gas. From examining Figures 19 and 20, it is also evident that the gas particles begin their runaway collapse with these characteristic values, to swiftly attain a temperature of $T \sim 1000$ K at the threshold density of $n = 10^8 \text{ cm}^{-3}$, at which point they are incorporated into a sink particle (i.e., a clump).

We turn next to the discussion of how the high-density clumps subsequently evolve, and of the processes through which they grow in mass, the accretion of surrounding diffuse material and the merging of clumps.

4.3. Later Evolution

At the end of the free-fall phase, the primordial cloud has fragmented into clumps with initial masses of $M_{Cl} \sim 10^2 - 10^3 M_\odot$. These clumps are the basic elements in the building-up of a spectrum of masses through the processes of accretion and merging. To address the complex dynamics which is involved in the shaping of the mass function, it is essential to be able to follow the systems' evolution over a few dynamical timescales. The technique of creating sink particles allows us to do so, which is another important advantage of our approach.

In the following, we first discuss the physics of accretion and merging, and then the resulting distribution of clump masses.

4.3.1. Accretion and Merging of Clumps

The next question to ask is: *What determines the fraction of gas which ends up in high-density clumps, and how does the difference in this quantity between the various simulations arise?* With $M_B = 10^5 M_\odot$ being the total amount of gas, and $t_{dyn} \sim 10^7$ yr the initial dynamical timescale of the DM halo, the overall rate of conversion between diffuse gas and clumps can be estimated

to be $\dot{M}_{conv} \simeq M_B/t_{dyn} \simeq 10^{-2} M_\odot \text{ yr}^{-1}$. The conversion rate, \dot{M}_{conv} , sets an upper limit to the star formation rate (SFR). Feedback effects from the developing proto-stars are expected to limit the SFR to a somewhat smaller value which at present is not known with any certainty.

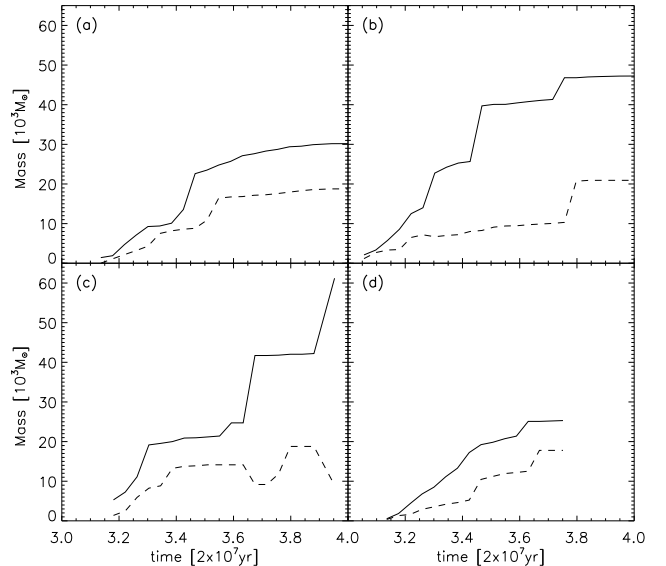


FIG. 21.— Growth of clumps in different runs. *Solid line*: Mass of most massive clump vs. time. *Dashed line*: Mass of second most massive clump vs. time. Mass is plotted in units of $10^3 M_\odot$, and time in 2×10^7 yr, which corresponds to the initial dynamical timescale. (a) Run A: Fiducial case. (b) Run C: Low-spin case. (c) Run E: $P(k) \propto k^0$. (d) Run K: Different realization of $P(k) \propto k^{-3}$. A rapid rise in mass (a ‘step’) corresponds to a merger with another clump, whereas a phase of slow and steady growth is due to accretion of diffuse gas. Notice the similarity in panels (a) and (d), with two dominant clumps surviving without further merging. The simulations in panels (b) and (c), corresponding to runs which result in a more centrally concentrated morphology, on the other hand, build up one very massive clump by successive merger events.

The clumps are comprised of gas which at some point has become Jeans unstable, and which has been drawn from the reservoir of cooled gas at the characteristic values of temperature and density, $T \sim$ a few 100 K and $n \simeq 10^3 - 10^4 \text{ cm}^{-3}$. In approximate pressure equilibrium with the cooled gas, a second, hot phase has formed at $T \sim 10^4$ K and $n \sim 10^1 \text{ cm}^{-3}$. Whatever material resides in this hot phase is not available for the formation of clumps. The total amount of cooled gas is typically $M_{cool} \sim 8 - 9 \times 10^4 M_\odot$. Once there is not enough gas left to overwhelm the opposing pressure, i.e., $M < M_J$, the Jeans instability ceases. If \bar{M}_J is the average Jeans mass at the moment of virialization, where the average includes all SPH particles which have been able to cool, the baryonic mass fraction in clumps is approximately given by

$$f_{Cl} \simeq \frac{M_{cool} - \bar{M}_J}{M_B} \quad (36)$$

In Table 4, we summarize the resulting conversion efficiency for three different simulations. The two simulations (Runs C and E) with a more concentrated gas morphology and correspondingly higher gas density are characterized by $f_{Cl} \sim 0.7$, as compared to $f_{Cl} \sim 0.5$ in the case of the less centrally concentrated gas configuration in Runs A and K. As can be seen, equation (36) nicely describes the

numerical results. All runs have a similar average temperature $\bar{T} \sim 300$ K, but the average gas density is an order of magnitude larger in Runs C and E. For these latter two simulations, therefore, the corresponding Jeans mass is smaller, and less of the cooled gas is left behind in a pressure supported state. In general, the conversion efficiency f_{Cl} increases with the central concentration and density of the gas. The larger central concentration is due to the low degree of angular momentum in Run C, and to the absence of a significant deviation from spherical symmetry in Run E. The fraction f_{Cl} constitutes an upper limit for the star formation efficiency (SFE), with the same degree of uncertainty as in the case of \dot{M}_{conv} and the SFR.

In Figure 21, we show how the two most massive clumps grow in mass for four different simulations, corresponding to the cases in Table 4. The clumps are formed with initial masses close to $M \sim 10^3 M_\odot$, and then gain in mass by the slow accretion of surrounding gas, and by merging with other clumps. Both mechanisms can be clearly discerned in the figure, where the merging events correspond to the step-like, sudden increase in mass. It is evident that there is significant merging activity in the high-density simulations (Runs C and E), whereas in Runs A and K, the clumps at late times only grow by steady accretion. This difference can be understood by considering the timescale for the collision of clumps, t_{coll} , and the corresponding collision rate (e.g., Bonnell et al. 1998)

$$\frac{1}{t_{coll}} = 16\sqrt{\pi}n_{Cl}vr_{acc}^2 \left[1 + \frac{GM_{Cl}}{2v^2r_{acc}} \right]. \quad (37)$$

Here, n_{Cl} is the number density of clumps, v the velocity dispersion, r_{acc} the accretion radius, and M_{Cl} the mass of a clump. The second term in the brackets is the Safronov number, describing the effect of gravitational focusing. Estimating the accretion radius as $r_{acc} \simeq 2h_{Cl} \simeq 0.1$ pc (see Section 3.2), and taking the clump mass to be $M_{Cl} \simeq 20,000M_\odot$, the result of evaluating equation (37) is summarized in Table 5. We accordingly expect of order 5 merger events in the high-density simulations (Runs C and E), as opposed to only 1 event in the low-density cases (Runs A and K). As can be seen in Figure 21, this prediction is borne out in the numerical simulations. A clump can become very massive by undergoing multiple mergers, up to $\sim 50,000M_\odot$ in Run C, and $\sim 60,000M_\odot$ in Run E. This runaway growth of one central clump is analogous to the evolution of a supergiant cD galaxy in the center of rich clusters of galaxies. From Figure 21, it is evident that at late evolutionary stages, clumps grow in mass mainly by merging with other clumps. In comparison, accretion of surrounding gas is a rather inefficient process.

4.3.2. Distribution of Clump Masses

In this section, we discuss the clump mass spectrum which results from the complex dynamics of merging and accretion described above. Although the initial masses of the clumps are close to $\sim 10^3 M_\odot$, rather independent of the initial conditions, the subsequent evolution of the clumps proceeds differently from case to case. As we have seen, the efficiency of merging is very sensitive to the central density of the post-virialization cloud. Despite the existence of a characteristic mass scale for Population III star formation, the mass spectrum, being determined by

the merging history of the clumps, is therefore expected to vary significantly. In the following, we investigate how the distribution of clump masses depends on the initial conditions. For each simulation, the gas and clump morphology is shown at a late evolutionary stage, where most of the available, cooled gas has already been incorporated into clumps.

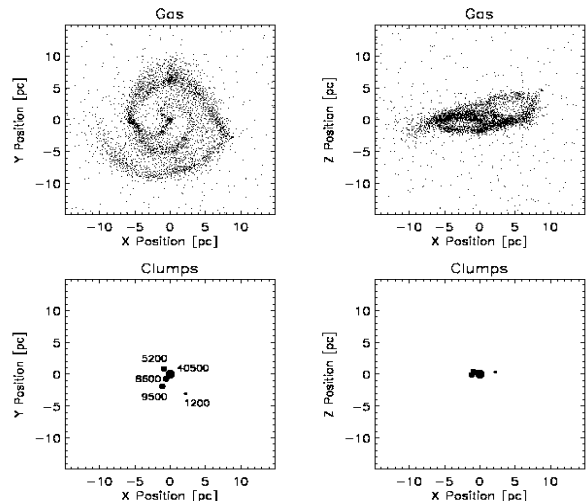


FIG. 22.— Run C: Low-spin case at $z = 28.9$. *Top row:* The remaining gas in the diffuse phase. *Bottom row:* Distribution of clumps. The numbers next to the dots denote clump mass in units of M_\odot . *Left panels:* Face-on view. *Right panels:* Edge-on view. The length of the box is 30 pc. Dominated by a massive clump of $\sim 40,000M_\odot$, comprising $\sim 40\%$ of the initially present gas, a compact, disk-like feature has formed in the center of the DM potential.

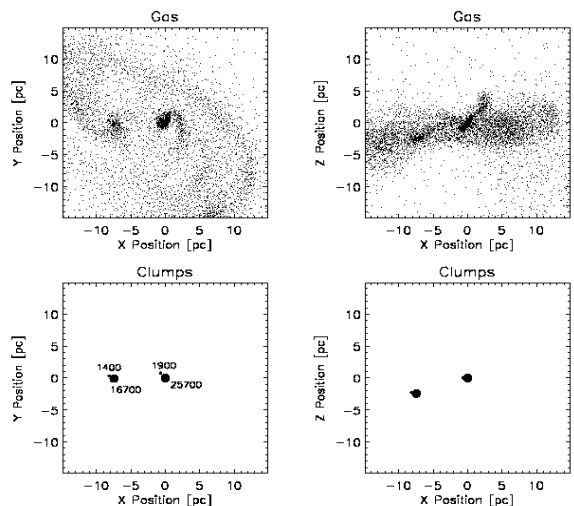


FIG. 23.— Run A: Intermediate-spin case at $z = 28.9$. The manner of presentation is the same as in Figure 22. Compared to the low-spin case, the gas has settled into a less regular, more extended configuration with two dominant clumps of mass close to $20,000M_\odot$. During the subsequent evolution, the clumps survive without merging, and grow in mass only slightly by accretion of surrounding gas.

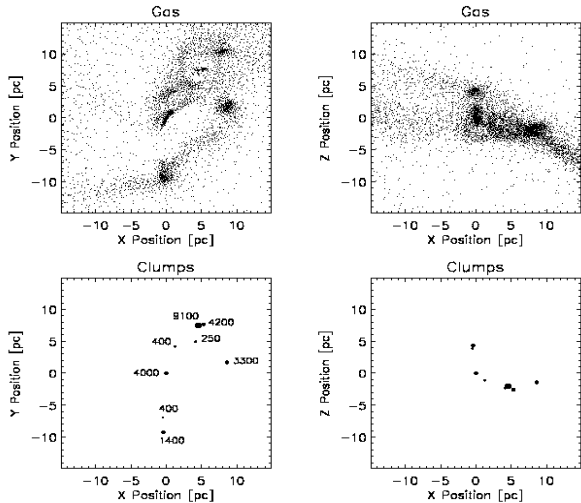


FIG. 24.— Run D: High-spin case at $z = 25.5$. The manner of presentation is the same as in Figure 22. Notice that here the situation is shown at a much later instant, reflecting the delayed conversion of the diffuse gas into clumps. The gas morphology is highly irregular and dispersed. In this case, no very massive clumps have formed, but instead a number of clumps with masses of a few $10^3 M_\odot$.

The total angular momentum of a halo proves to be a very important parameter in determining the mass spectrum of the clumps. To demonstrate this, we consider the simulations with low, intermediate, and high initial spin in Figures 22, 23, and 24, respectively. As can be clearly seen, the mass of the dominating clump decreases with increasing spin. This clump mass - spin relation has a straightforward explanation in the lower central density of the higher spin simulations, and the corresponding reduction in the merger rate. Hence, high-density clumps with masses $M \gtrsim 50,000 M_\odot$ can form in the center of the lowest-spin halos. These massive clumps might conceivably lead to the formation of seed black holes for future quasar activity. Eisenstein & Loeb (1995) have investigated a scenario along these lines, emphasizing the cosmological importance of the low-spin systems.

The emergence of such very massive (cD like) clumps is due to the efficient outward transport of angular momentum via tidal torques. Although we do not include the effect of any external tidal fields, and have to insert the angular momentum explicitly at the beginning of the simulation, the subsequent dynamics does lead to internal tidal fields. In cases where there is such a "cD behavior", the effect responsible for it therefore seems to be modelled in a physically consistent way. Interestingly, a high degree of central concentration is also found in the simulation of ABN2000 who have self-consistently included cosmological tidal fields. As we discuss below, the neglect of any proto-stellar feedback seems to be the more crucial factor in accounting for the emergence of very massive clumps.

Earlier on, we have mentioned that the two simulations (Runs A and K) with a different realization of the k^{-3} power spectrum, and all other parameters being equal, lead to a rather different DM and gas morphology at the moment of virialization. During the later stages of the evolution, however, these simulations converge to a similar state. In both simulations, the morphology is dominated

by two clumps with masses close to $\sim 20,000 M_\odot$. The overall features of the mass spectrum, therefore, do not seem to depend significantly on the random initialization of the DM fluctuations. The late-time morphology in the simulation with a high baryon fraction (Run L) is characterized by the largest fraction of gas in clumps, $\sim 75\%$, and has a central cD clump of mass $M \sim 200,000 M_\odot$, which has gobbled up a remarkable one-half of the total gas mass. As we have pointed out before, the case of a high baryon fraction behaves distinctly different from the low Ω_B simulations in that gravitational instability is already triggered during the initial free-fall phase. Now we see that Run L is also distinguished by an extremely top-heavy spectrum of clump masses. This case serves as an illustration for what happens when the relative balance of gas pressure and self-gravity is shifted in favor of the latter.

To assess the possible role of HD cooling in the evolution of the primordial gas, we compare Run A, which does include HD cooling, and Run F, which does not. Otherwise, the two cases have identical initial conditions. We find that the gas and clump morphologies, as well as the thermodynamic behavior in the T vs. n plane, are overall very similar. Slight differences, however, do exist in the way the gas fragments, and in the resulting clump masses. Cooling due to the HD molecule, and the corresponding chemistry of its formation and destruction, should therefore be included for completeness, even though it does not appear to be of pre-eminent importance in the parameter regime considered here. In our simulations, we have assumed a deuterium abundance of $n_D = 4 \times 10^{-5} n_H$, but we have carried out a test calculation with a ten times higher abundance. With such a high D abundance, the thermal evolution of the gas proceeds very differently. Cooling now is so efficient that the gas quickly settles down to the temperature of the CMB, and the corresponding Jeans mass is reduced below the resolution limit of that simulation, $M_{res} \sim 200 M_\odot$. If deuterium were indeed that abundant, the characteristic mass scale of $\sim 10^3 M_\odot$ would then disappear, since it derives from the properties of H_2 (see Section 2). Our adopted value of $n_D/n_H = 4 \times 10^{-5}$, however, seems to be a conservatively high choice, according to recent observations of high-redshift absorption systems (e.g., Burles & Tytler 1998).

Finally, we discuss the cumulative distribution of clump masses. We consider the average of all simulations with DM fluctuations imprinted according to a k^{-3} spectrum, initial spin $\omega = 0.2$, and a total halo mass of $2 \times 10^6 M_\odot$. As we have discussed above, varying these parameters leads to a significant change in the distribution of clump masses, and we have therefore included in the averaging only the cases with these fiducial values. We evaluate the number of clumps per unit logarithmic mass, and compare this to the Salpeter case of the present-day stellar IMF, $dN/d \log m \propto m^{-1.35}$. It turns out that the resulting mass spectrum is remarkably flat, and that the halos in our simulations are very efficient in building up very massive clumps, up to a few times $10^4 M_\odot$.

This mass spectrum has to be taken *cum grano salis*, and important caveats apply. First, recall that clumps are born with masses close to $\sim 10^3 M_\odot$, and only subsequently reach higher masses through successive mergers and accretion. For these mechanisms to be effective, there

has to be sufficient time. Typical merging timescales are of order a few 10^6 yr, during which time the first stars in the halo might have already evolved far enough to explode as supernovae, thereby considerably disturbing the remaining gas in the halo. In general, the neglect of any feedback effects constitutes the major shortcoming in our treatment of these later evolutionary stages. Up to the point of forming the first clump, and possibly the first few, all the relevant physics is in principle known. It is only towards the later stages in the evolution that the physical basis of the simulations becomes increasingly uncertain. It is also worth remembering that only those processes are allowed for in our numerical treatment which tend to *increase* the mass of a clump. This introduces a bias towards higher mass in the resulting mass spectrum.

Having stated all these provisions, it is nevertheless remarkable how efficient the Population III halos are in building up clumps of very high mass. The assessment of how relevant this finding is for an understanding of the stellar IMF, has to await a more realistic treatment of the complex physics of accretion from a dust-free envelope, the merging of subcondensations, and the various feedback effects.

5. SUMMARY AND CONCLUSIONS

We have investigated the collapse and fragmentation of primordial, metal-free gas. The gas is embedded in dark matter halos of mass close to $\sim 10^6 M_\odot$ which virialize at redshifts $z \simeq 20 - 30$. Due to the low virial temperatures in these halos of a few 1000 K, cooling can only proceed via H_2 . We find that for these systems there exists a preferred region in parameter space. The primordial gas does attain characteristic temperatures of a few 100 K, and densities of $\sim 10^3 - 10^4 \text{ cm}^{-3}$. These values have their physical explanation in the microphysics of H_2 cooling, related to the minimum temperature that can be reached via H_2 , and to the critical density where the cooling rate changes from being proportional to n^2 to an only linear dependence on density. This change in the cooling rate reflects the transition from NLTE to LTE level populations of the hydrogen molecule. With these values of temperature and density, the corresponding characteristic Jeans mass is $M_J \sim 10^3 M_\odot$. At some point during the simulation, the gas becomes gravitationally unstable, and forms high density ($n > 10^8 \text{ cm}^{-3}$) clumps with initial masses close to the characteristic Jeans scale of $\sim 10^3 M_\odot$. This is a very robust result, and is quite independent of the initial conditions. This suggests that Population III star formation might have favored massive stars, possibly even very massive ones with $M \gtrsim 100 M_\odot$.

In contrast to this robust nature of the thermodynamics, the resulting morphology is a somewhat accidental feature of our simulations, varying substantially between different random realizations of the initial DM density field.

Although the clumps form initially with similar masses close to the characteristic value of $\sim 10^3 M_\odot$, their further evolution is very sensitive to the initial conditions. Clumps grow in mass through accretion of surrounding gas, and merging with other clumps. Both mechanisms sensitively depend on the central gas density. We now discuss the dependence of the resulting clump masses on the most important parameters.

Total halo mass.— With increasing mass of the DM halo,

the clump masses also tend to increase. Initial clump masses are close to $M_{Cl} = 400 M_\odot$ in the $10^5 M_\odot$ halo, and approximately twice as massive in the $10^6 M_\odot$ cases. In addition, a few clumps form almost simultaneously in the more massive halos, whereas only a single one forms in the center of the ‘marginal’ ($10^5 M_\odot$) halo.

Angular momentum.— The growth of a clump by accretion and merging is very sensitive to the amount of angular momentum initially imparted to the DM halo. Lower spin halos acquire denser central configurations which favor the frequent merging of clumps. Clump masses can then become very large (up to a few times $10^4 M_\odot$).

Collapse redshift.— The efficiency of accretion and merging is also increased in runs with higher collapse redshifts, which is again a direct consequence of the enhanced overall density. As a result, clump masses tend to be larger at higher redshift.

Baryon fraction.— In the simulation with a larger fraction of baryons relative to the DM, runaway collapse is already triggered during the initial free-fall collapse, and resulting clump masses are systematically higher.

Recently, ABN2000 have used the adaptive mesh refinement (AMR) method to study the formation of the first stars. These authors start their calculation with cosmological initial conditions, resulting in the most realistic treatment of the problem to date. Since they have presented only one case, however, it is not easy to ascertain the robustness of their result, and this is the specific advantage of our exploratory approach. We agree on the existence of characteristic values for the density and temperature of the primordial gas, deriving from the microphysics of H_2 cooling. ABN2000 give an upper limit for the final mass of a Population III star of $200 M_\odot$, whereas the distribution of clump masses in our work suggests that somewhat higher masses, perhaps up to $1000 M_\odot$, are possible. ABN2000 have criticised our earlier work (Bromm et al. 1999) in that the rather smooth gaseous disk found in that study is unrealistic and an artefact of the assumed top-hat initial conditions. Most of the cases presented here, however, do not yield such a regular disk morphology, and result in very irregular configurations that are dominated by filaments and knots. Furthermore, our Run H, corresponding to a less massive halo ($M_{tot} = 10^5 M_\odot$), is in good overall agreement with the simulation of ABN2000 as to the morphology and the fact that only one clump forms in the center of the DM halo.

Although one has a reasonably strong case in arguing that all the relevant physics is in hand to follow the collapse of the primordial gas up to the formation of the first high-density region, this fortunate circumstance gives way to growing uncertainty afterwards. Two of the most tantalizing questions are the following. *How effective is the energy output from the protostellar core in shutting off accretion from a very massive, dust-free envelope?* On this question hinges the ultimate mass scale of the first stars, and it is at present far from being answered. In Paper II, however, we will further address the question of the upper mass limit of a Population III star. This upper mass limit is important for testing the idea that Population III stars might be the precursors of black holes of mass $\sim 10^3 M_\odot$, intermediate between stellar and supermassive ones (e.g., Madau & Rees 2001). *What is the IMF of Population III stars?* In our simulations, we have seen how the

mass spectrum of clumps is built up through the complex interplay of merging and accretion, and that the resulting mass spectrum is very flat compared to the Salpeter IMF. It is difficult to tell, however, how this result relates to the stellar IMF, since again we are hampered by our neglect of any negative feedback effects, which are almost certain to play an important role in determining the IMF. Both questions highlight the importance of feedback effects for a deeper understanding of the star formation process.

We are grateful to A. Ferrara, A. Loeb, M. Norman, and M. Rees for comments and stimulating discussions. We would like to thank Z. Haiman and A. Loeb for providing us with their chemical reaction rates and L. Hernquist for making available to us a version of TREESPH. Support from the NASA ATP grant NAG5-7074 is gratefully acknowledged.

APPENDIX

A. N-BODY SOLVER

In the following, we briefly discuss the basic ideas of solving the gravitational N-body problem, and refer the reader to Hernquist & Katz (1989; HK89 henceforth), Aarseth (1994), and Barnes (1998) for further details. In the context of TREESPH, the treatment of self-gravity is almost identical for the dark matter and the gas, since both components are represented by particles which constitute a Monte-Carlo sampling of the underlying fluids. Let us first turn to the dark matter, and describe the minor modifications for the gas at the end of this section.

Since particle methods are Lagrangian by design, mass is conserved automatically, thus rendering the equation of continuity superfluous. The equation of motion for DM particle i simply reads:

$$\frac{d\vec{v}_i}{dt} = -(\nabla\Phi)_i \quad . \quad (\text{A1})$$

The gravitational potential is given by the standard solution to Poisson's equation:

$$\Phi_i = -G \int \frac{\rho(\vec{r})}{|\vec{r} - \vec{r}_i|} d^3r \quad . \quad (\text{A2})$$

If one now were to assume the case of true point masses, the density could be written as

$$\rho(\vec{r}) = \sum_j m_j \delta(\vec{r} - \vec{r}_j) \quad , \quad (\text{A3})$$

with $\delta(\vec{r})$ being the Dirac delta-function. Inserting equ. (A3) into equ. (A2), and applying the gradient operator, yields the familiar result for the gravitational acceleration of particle i :

$$-(\nabla\Phi)_i = G \sum_{j \neq i} m_j \frac{\vec{r}_j - \vec{r}_i}{|\vec{r}_j - \vec{r}_i|^3} \quad . \quad (\text{A4})$$

This straightforward procedure has two crucial shortcomings which we now discuss in turn, together with the adopted remedies.

First, there is the problem of discreteness on very small scales. Close encounters of particles lead to collisional two-body relaxation, which is clearly undesirable in modelling a smooth fluid. Therefore, gravitational forces have to be softened on scales close to the interparticle distance. In TREESPH, this is accomplished by replacing the singular Dirac delta-function with the spherical spline kernel W , used in the SPH formalism (see Appendix B):

$$\rho(\vec{r}) = \sum_j m_j W(\vec{r} - \vec{r}_j; \epsilon) \quad . \quad (\text{A5})$$

The result of inserting this *Ansatz* into equ. (A2) is given by HK89. Due to its compact nature ($W(r) = 0$ for $r > 2\epsilon$), the use of this kernel reproduces the Kepler-potential exactly for $r > 2\epsilon$. Each particle has its own softening length, ϵ_i , which is adjusted such that there is a constant number of neighbors, N_s , in a softening volume: $N_s \simeq n_i (2\epsilon_i)^3$, where n_j is the local particle density. In our simulations, we have set $N_s = 16$.

The second problem concerns the computational expense of determining the gravitational forces, which scales as $O(N^2)$ for the direct summation in equ. (A4). An ingenious way to overcome this prohibitive cost has been developed by Barnes & Hut (1986). Their method organizes the particles into a recursive tree structure, such that individual particles correspond to the leaves of the tree, neighboring particles in space to leaves on the same branch, and the system as a whole to the root of the tree. Each node of this tree represents a cubical cell in real space. The leaves correspond to the smallest cells, containing only one particle, higher-level branching points to larger cells, containing groups of particles, and the root to the overall system box, including all the particles. This procedure is completely adaptive, and can accommodate arbitrary

geometries. To finally calculate the gravitational force on a given particle, the tree is traversed from the root down. For each node (cell) of size s and distance d to the particle, an accuracy criterion is evaluated:

$$\frac{s}{d} < \theta \quad , \quad (\text{A6})$$

where the parameter θ determines the desired precision, and is chosen to be $\theta = 0.8$ in our simulations. If this criterion is fulfilled, all the particles in the given cell are treated as a single group whose gravitational influence is approximately described by performing a multipole expansion of the respective potential, in our case up to quadrupole order. If, on the other hand, the accuracy criterion is not met, the tree is walked down to the next level of refinement. This procedure is repeated recursively, until either the criterion in equ. (A6) is fulfilled, or the tree descent has reached the level of individual particles (the leaves). In consequence, forces are calculated accurately but expensively only for nearby particles, and approximately but fast for more remote ones. Both the construction of the tree, and the subsequent descent of it, have a computational cost of only $O(N \log N)$, making simulations with larger numbers of particles possible.

The equation of motion is solved explicitly using a standard, time-centered leapfrog integrator. The position and velocity of particle i are updated according to:

$$\begin{aligned} \vec{r}_i^{n+1/2} &= \vec{r}_i^{n-1/2} + \vec{v}_i^n \Delta t_i + O(\Delta t_i^3) \\ \vec{v}_i^{n+1} &= \vec{v}_i^n + \vec{a}_i^{n+1/2} \Delta t_i + O(\Delta t_i^3) \end{aligned} \quad (\text{A7})$$

Here, superscripts denote timesteps. Velocities are stored at times which are offset by one-half a timestep from the positions and accelerations. This (leapfrog) characteristic guarantees the second-order accuracy of the algorithm. Each particle is allowed to have its individual timestep, Δt_i , which is chosen to fulfill the criterion

$$\Delta t_i \leq e_{tol} \frac{E_i}{a_i v_i} \quad . \quad (\text{A8})$$

E_i is the total energy of particle i , and e_{tol} the tolerance parameter which we have set to be $e_{tol} = 0.1$.

The gaseous component is treated in exactly the same way, with the exception that in this case the gravitational softening length is always equal to the SPH smoothing length (see below). In Figure 1, we demonstrate that the code does nicely reproduce the analytical top-hat solution, with total energy and angular momentum being conserved to better than 5%.

B. THE SPH METHOD

We briefly describe the basic principles of the smoothed particle hydrodynamics (SPH) method, and give an intuitive motivation for the resulting equations. Further details are given in, e.g., Benz (1990), Monaghan (1992), Müller (1998), and HK89.

The fluid is sampled by discrete particles, representing fluid elements. To model a continuous medium, the mass of a particle is smoothed according to

$$\rho(\vec{r}) = \sum_j m_j W(\vec{r} - \vec{r}_j; h) \quad (\text{B1})$$

The smoothing kernel, W , is strongly peaked at $\vec{r} = \vec{r}_j$, and normalized to give $\int W d^3 r = 1$, where integration is over all space. TREESPH implements the spherically symmetric spline kernel

$$W(r, h) = \frac{1}{\pi h^3} \begin{cases} 1 - \frac{3}{2} \left(\frac{r}{h}\right)^2 + \frac{3}{4} \left(\frac{r}{h}\right)^3, & 0 \leq \frac{r}{h} \leq 1 \\ \frac{1}{4} \left[2 - \left(\frac{r}{h}\right)\right]^3, & 1 \leq \frac{r}{h} \leq 2 \\ 0, & \frac{r}{h} \geq 2 \end{cases} \quad (\text{B2})$$

The smoothing length, h , describes the spatial extent of a given SPH particle. TREESPH assigns variable smoothing lengths to each particle, thereby introducing an adaptive spatial resolution, such that there is a (roughly) constant number of particles, N_{neigh} , within the smoothing volume. We have adopted $N_{neigh} = 32$ in our work. Now, one can easily find smoothed estimates for any variable $A(\vec{r})$. Starting with the interpolation formula

$$A(\vec{r}) = \int A(\vec{r}') W(\vec{r} - \vec{r}'; h) d^3 r' \quad , \quad (\text{B3})$$

and assigning an effective volume to each particle j via $m_j \simeq \rho(\vec{r}_j) \Delta^3 r_j$, one can approximate the integral as

$$A(\vec{r}) \simeq \sum_j A_j \frac{m_j}{\rho_j} W(\vec{r} - \vec{r}_j; h) \quad , \quad (\text{B4})$$

where $A_j = A(\vec{r}_j)$, and $\rho_j = \rho(\vec{r}_j)$. The crucial advantage of the SPH method lies in the fact that it does not need a grid to evaluate spatial derivatives. To illustrate this point, let us apply the gradient operator to equ. (B4):

$$\nabla_r A(\vec{r}) \simeq \sum_j A_j \frac{m_j}{\rho_j} \nabla_r W(\vec{r} - \vec{r}_j; h) \quad . \quad (\text{B5})$$

Consequently, taking spatial derivatives in SPH only involves the analytical differentiation of the kernel function which is specifically chosen to admit this.

Next, we present the SPH equations as used in our numerical work. We give heuristic arguments for their appearance, and refer to the cited literature for the formal derivations. The equation of continuity is again automatically fulfilled due to the Lagrangian nature of the SPH method. The equation of motion for particle i reads

$$\frac{d\vec{v}_i}{dt} = -(\nabla\Phi)_i - \frac{\nabla P_i}{\rho_i} + \vec{a}_{\text{sh},i} \quad . \quad (\text{B6})$$

To find a smoothed estimate for the pressure gradient, one could naively write, using equ. (B5):

$$\frac{\nabla P_i}{\rho_i} = \sum_j m_j \frac{P_j}{\rho_i \rho_j} \nabla_i W(r_{ij}; h_i) \quad .$$

This form, however, does not conserve linear and angular momentum. To satisfy Newton's third law, one wants an expression which is symmetric with respect to any given pair of particles, i and j . From amongst the options given in TREESPH, we have chosen to work with

$$\frac{\nabla P_i}{\rho_i} = \sum_j 2 \frac{\sqrt{P_i P_j}}{\rho_i \rho_j} m_j \frac{1}{2} [\nabla_i W(r_{ij}; h_i) + \nabla_i W(r_{ij}; h_j)] \quad . \quad (\text{B7})$$

The symbol ∇_i denotes derivation with respect to \vec{r}_i , and $r_{ij} = |\vec{r}_i - \vec{r}_j|$. The pressure is given by the ideal gas law

$$P_i = \rho_i \frac{k_B T}{\mu m_H} = (\gamma - 1) u_i \rho_i \quad . \quad (\text{B8})$$

μ is the (dimensionless) mean molecular weight, γ the ratio of specific heats, and u_i the specific internal energy (in erg g^{-1}). For an almost neutral gas consisting of helium and atomic hydrogen, one has $\mu \simeq 1.2$, and $\gamma = 5/3$. The corresponding symmetric estimate for the viscous acceleration $\vec{a}_{\text{sh}} = -\nabla Q_{\text{eff}}/\rho$ can be written as:

$$\frac{\nabla Q_{\text{eff},i}}{\rho_i} = \sum_j \Pi_{ij} m_j \frac{1}{2} [\nabla_i W(r_{ij}; h_i) + \nabla_i W(r_{ij}; h_j)] \quad . \quad (\text{B9})$$

Finding Π_{ij} , a symmetric estimate for Q_{eff}/ρ^2 , relies on the following conceptual steps. First, let us specify the pseudo-viscous pressure, $Q_{\text{eff}} = -\rho \nu_{\text{eff}} \nabla \cdot \vec{v}$, arising from the presence of an artificial viscosity. The latter has two contributions: A bulk viscosity

$$\nu_{\text{eff}} = \alpha l c_s \quad , \quad (\text{B10})$$

and a von Neumann-Richtmyer viscosity

$$\nu_{\text{eff}} = -\beta l^2 \nabla \cdot \vec{v} \quad . \quad (\text{B11})$$

Here, l is a characteristic length, c_s the sound speed, and α, β are parameters of order unity. The resulting pseudo-viscous pressure can then be written as

$$Q_{\text{eff}} = -\alpha \rho c_s l \nabla \cdot \vec{v} + \beta \rho l^2 (\nabla \cdot \vec{v})^2 \quad . \quad (\text{B12})$$

A symmetric estimate for $l \nabla \cdot \vec{v}$ is given by

$$\mu_{ij} = \begin{cases} \frac{h_{ij} \vec{v}_{ij} \cdot \vec{r}_{ij}}{r_{ij}^2 + 0.01 h_{ij}^2} & \text{if } \vec{v}_{ij} \cdot \vec{r}_{ij} \leq 0 \\ 0 & \text{otherwise} \end{cases} \quad , \quad (\text{B13})$$

where $\vec{v}_{ij} = \vec{v}_i - \vec{v}_j$, and $h_{ij} = (h_i + h_j)/2$. Assembling these ingredients, one finally has

$$\Pi_{ij} = \frac{-\alpha \mu_{ij} c_{ij} + \beta \mu_{ij}^2}{\rho_{ij}} \quad , \quad (\text{B14})$$

where $\rho_{ij} = (\rho_i + \rho_j)/2$, and $c_{ij} = (c_{s,i} + c_{s,j})/2$. In our work, we use $\alpha = 1$ and $\beta = 2$. We have experimented with alternative prescriptions for the artificial viscosity (as given by HK89), and find that our results do not depend on this

choice. Certain morphological features such as pronounced rings, however, could be due to an unphysical viscosity that can arise in simulations with a relatively small number of particles. The equation of motion is now fully specified, and is solved with the leapfrog integrator. The stability of the integration is enforced by the classic Courant condition:

$$\Delta t_i \leq \frac{h_i}{c_{s,i} + h_i |\nabla \cdot \vec{v}_i|} \quad . \quad (\text{B15})$$

HK89 give a version of the criterion which also takes into account the artificial viscosity. The appropriate timestep for a given SPH particle is the minimum of the Courant timestep and the one given by the energy criterion, equ. (A8).

Along similar lines, HK89 write the smoothed form of the thermal energy equation, equ. (5), as

$$\begin{aligned} \frac{du_i}{dt} = \sum_j m_j \left(\frac{\sqrt{P_i P_j}}{\rho_i \rho_j} + \frac{1}{2} \Pi_{ij} \right) \vec{v}_{ij} \\ \cdot \frac{1}{2} [\nabla_i W(r_{ij}; h_i) + \nabla_i W(r_{ij}; h_j)] + \left(\frac{\Gamma - \Lambda}{\rho} \right)_i \quad . \end{aligned} \quad (\text{B16})$$

In the presence of radiative cooling and heating, this equation cannot be solved explicitly, since the corresponding radiative timescales are typically much shorter than the dynamical time which sets the timestep for the equation of motion. The thermal energy equation is therefore integrated implicitly, using the standard second-order trapezoidal rule (see HK89 for further details).

REFERENCES

- Aarseth, S. J. 1994, in *Galactic Dynamics and N-Body Simulations*, ed. G. Contopoulos, N. K. Spyrou, & L. Vlahos (Berlin: Springer), 277
- Abel, T., Anninos, P., Norman, M. L., & Zhang, Y. 1998, *ApJ*, 508, 518
- Abel, T., Bryan, G. L., & Norman, M. L. 2000, *ApJ*, 540, 39
- Anninos, P., & Norman, M. L. 1996, *ApJ*, 460, 556
- Anninos, P., Zhang, Y., Abel, T., & Norman, M. L. 1997, *NewA*, 2, 209
- Barnes, J. E., & Hut, P. 1986, *Nature*, 324, 446
- Barnes, J., & Efstathiou, G. 1987, *ApJ*, 319, 575
- Barnes, J. E. 1998, in *Saas-Fee Advanced Course 26. Galaxies: Interactions and Induced Star Formation*, ed. D. Friedli, L. Martinet, & D. Pfenniger (Berlin: Springer)
- Bate, M. R., Bonnell, I. A., & Price, N. M. 1995, *MNRAS*, 277, 362
- Bate, M. R., & Burkert, A. 1997, *MNRAS*, 288, 1060
- Beers, T. C. 2000, in "The First Stars", *ESO Astrophysics Symposia*, ed. A. Weiss, T. Abel, & V. Hill (Berlin: Springer), 3
- Benz, W. 1990, in *Proceedings of the NATO Advanced Research Workshop on The Numerical Modelling of Nonlinear Stellar Pulsations*, ed. J. R. Buchler (Dordrecht: Kluwer), 269
- Blumenthal, G. R., Faber, S. M., Primack, J. R., & Rees, M. J. 1984, *Nature*, 311, 517
- Bonnell, I. A., Bate, M. R., & Zinnecker, H. 1998, *MNRAS*, 298, 93
- Bromm, V., Coppi, P. S., & Larson, R. B. 1999, *ApJ*, 527, L5
- Burles, S., & Tytler, D. 1998, *ApJ*, 507, 732
- Carlberg, R. G. 1981, *MNRAS*, 197, 1021
- Carr, B. J., Bond, J. R., & Arnett, W. D. 1984, *ApJ*, 277, 445
- Cen, R. 1992, *ApJS*, 78, 341
- Chen, H. W., Lanzetta, K. M., & Pascarella, S. 1999, *Nature*, 398, 586
- Ciardi, B., Ferrara, A., Governato, F., & Jenkins, A. 2000, *MNRAS*, 314, 611
- Copi, C. J., Schramm, D. N., & Turner, M. S. 1995, *Phys. Rev. Lett.*, 75, 3981
- Couchman, H. M. P., & Rees, M. J. 1986, *MNRAS*, 221, 53
- Cowie, L. L., & Songaila, A. 1998, *Nature*, 394, 44
- Dodelson, S., & Jubas, J. M. 1995, *ApJ*, 439, 503
- Eisenstein, D. J., & Loeb, A. 1995, *ApJ*, 443, 11
- Fan, X. et al. 2000, *AJ*, 120, 1167
- Ferrara, A. 1998, *ApJ*, 499, L17
- Flower, D. R., Le Bourlot, J., Pineau des Forêts, G., & Roueff, E. 2000, *MNRAS*, 314, 753
- Forrey, R. C., Balakrishnan, N., Dalgarno, A., & Lepp, S. 1997, *ApJ*, 489, 1000
- Fuller, T. M., & Couchman, H.M.P. 2000, *ApJ*, 544, 6
- Galli, D., & Palla, F. 1998, *A&A*, 335, 403
- Gunn, J. E., & Peterson, B. A. 1965, *ApJ*, 142, 1633
- Haiman, Z., Thoul, A. A., & Loeb, A. 1996, *ApJ*, 464, 523
- Haiman, Z., & Loeb, A. 1997, *ApJ*, 483, 21
- Hernquist, L., & Katz, N. 1989, *ApJS*, 70, 419
- Hindmarsh, A. C. 1983, in *Scientific Computing*, ed. R. S. Stepleman et al. (Amsterdam: North Holland)
- Hollenbach, D., & McKee, C. F. 1979, *ApJS*, 41, 555
- Hu, E. M., Cowie, L. L., & McMahon, R. G. 1998, *ApJ*, 502, 99
- Hutchins, J. B. 1976, *ApJ*, 205, 103
- Jeans, J. H. 1902, *Phil. Trans. R. Soc.*, 199A, 49
- Kashlinsky, A., & Rees, M. J. 1983, *MNRAS*, 205, 955
- Kulsrud, R. M. 1997, in "Critical Dialogues in Cosmology", ed. N. Turok (Singapore: World Scientific), 328
- Larson, R. B. 1998, *MNRAS*, 301, 569
- Lawrence, C. R., Scott, D., & White, M. 1999, *PASP*, 111, 525
- Lepp, S., & Shull, J.M. 1983, *ApJ*, 270, 578
- Loeb, A., & Haiman, Z. 1997, *ApJ*, 490, 571
- Loeb, A. 1998, in *ASP Conf. Ser. 133, Science with the Next Generation Space Telescope*, ed. E. Smith & A. Koratkar (San Francisco: ASP), 73
- Loeb, A. 1999, in *ASP Conf. Ser. 193, The Hy-Redshift Universe: Galaxy Formation and Evolution at High Redshift*, ed. A.J. Bunker & W.J.M. van Breugel (San Francisco: ASP), 586
- Lynden-Bell, D. 1967, *MNRAS*, 136, 101
- Madau, P., & Rees, M.J. 2001, *ApJ*, 551, L27
- Martin, P.G., Schwarz, D.H., & Mandy, M.E. 1996, *ApJ*, 461, 265
- McDowell, M. R. C. 1961, *Observatory*, 81, 240
- Miralda-Escudé, J., & Rees, M. J. 1997, *ApJ*, 478, 57
- Miralda-Escudé, J., Haehnelt, M., & Rees, M. J. 2000, *ApJ*, 530, 1
- Monaghan, J. J. 1992, *ARA&A*, 30, 543
- Moore, B., Ghigna, S., Governato, F., Lake, G., Quinn, T., Stadel, J., & Tozzi, P. 1999, *ApJ*, 524, L19
- Müller, E. 1998, in *Saas-Fee Advanced Course 27. Computational Methods for Astrophysical Fluid Flow*, ed. O. Steiner & A. Gautschy (Berlin: Springer), 343
- Nakamura, F., & Umemura, M. 1999, *ApJ*, 515, 239
- Omukai, K., & Nishi, R. 1998, *ApJ*, 508, 141
- Ostriker, J. P., & Gnedin, N. Y. 1996, *ApJ*, 472, L63
- Padmanabhan, T. 1993, *Structure Formation in the Universe* (Cambridge: Cambridge Univ. Press), 273
- Palla, F., Salpeter, E. E., & Stahler, S. W. 1983, *ApJ*, 271, 632
- Peacock, J. A. 1999, *Cosmological Physics* (Cambridge: Cambridge Univ. Press), 381
- Press, W. H., Teukolsky, S. A., Vetterling, W. T., & Flannery, B. P. 1992, *Numerical Recipes in Fortran* (2nd ed.; Cambridge: Cambridge Univ. Press)
- Rees, M. J., & Ostriker, J. P. 1977, *MNRAS*, 179, 541
- Rees, M. J. 1999, in *AIP Conf. Proc. 470, After the Dark Ages: When Galaxies were Young (the Universe at 2 < z < 5)*, ed. S. S. Holt & E. Smith (Woodbury: AIP), 13
- Rees, M. J. 2000, *New Perspectives in Astrophysical Cosmology* (Cambridge: Cambridge Univ. Press), 36
- Sellwood, J. A. 1987, *ARA&A*, 25, 151
- Silk, J. 1977, *ApJ*, 211, 638
- Silk, J. 1983, *MNRAS*, 205, 705
- Tegmark, M., Silk, J., Rees, M. J., Blanchard, A., Abel, T., & Palla, F. 1997, *ApJ*, 474, 1
- Uehara, H., Susa, H., Nishi, R., Yamada, M., & Nakamura, T. 1996, *ApJ*, 473, L95

TABLE 1
 REACTION RATES FOR HYDROGEN SPECIES

	Reaction	Rate Coefficient (cm^3s^{-1})	Reference
(1)	$\text{H} + e^- \rightarrow \text{H}^+ + 2e^-$	$5.85 \times 10^{-11} T^{1/2} \exp(-157,809.1/T) (1 + T_5^{1/2})^{-1}$	1
(2)	$\text{H}^+ + e^- \rightarrow \text{H} + h\nu$	$8.40 \times 10^{-11} T^{-1/2} T_3^{-0.2} (1 + T_6^{0.7})^{-1}$	1
(3)	$\text{H} + e^- \rightarrow \text{H}^- + h\nu$	See expression in reference	2
(4)	$\text{H} + \text{H}^- \rightarrow \text{H}_2 + e^-$	1.30×10^{-9}	1
(5)	$\text{H}^- + \text{H}^+ \rightarrow 2\text{H}$	$7.00 \times 10^{-7} T^{-1/2}$	1
(6)	$\text{H}_2 + e^- \rightarrow \text{H} + \text{H}^-$	$2.70 \times 10^{-8} T^{-3/2} \exp(-43,000/T)$	1
(7)	$\text{H}_2 + \text{H} \rightarrow 3\text{H}$	See expression in reference	1
(8)	$\text{H}_2 + \text{H}^+ \rightarrow \text{H}_2^+ + \text{H}$	$2.40 \times 10^{-9} \exp(-21,200/T)$	1
(9)	$\text{H}_2 + e^- \rightarrow 2\text{H} + e^-$	$4.38 \times 10^{-10} \exp(-102,000/T) T^{0.35}$	1
(10)	$\text{H}^- + e^- \rightarrow \text{H} + 2e^-$	$4.00 \times 10^{-12} T \exp(-8750/T)$	1
(11)	$\text{H}^- + \text{H} \rightarrow 2\text{H} + e^-$	$5.30 \times 10^{-20} T \exp(-8750/T)$	1
(12)	$\text{H}^- + \text{H}^+ \rightarrow \text{H}_2^+ + e^-$	See expression in reference	1

TABLE 2
REACTION RATES FOR DEUTERIUM SPECIES

	Reaction	Rate Coefficient (cm^3s^{-1})	Reference
(1)	$\text{D}^+ + e^- \rightarrow \text{D} + h\nu$	$8.40 \times 10^{-11} T^{-1/2} T_3^{-0.2} (1 + T_6^{0.7})^{-1}$	1
(2)	$\text{D} + \text{H}^+ \rightarrow \text{D}^+ + \text{H}$	$3.70 \times 10^{-10} T^{0.28} \exp(-43/T)$	3
(3)	$\text{D}^+ + \text{H} \rightarrow \text{D} + \text{H}^+$	$3.70 \times 10^{-10} T^{0.28}$	3
(4)	$\text{D}^+ + \text{H}_2 \rightarrow \text{H}^+ + \text{HD}$	2.10×10^{-9}	3
(5)	$\text{HD} + \text{H}^+ \rightarrow \text{H}_2 + \text{D}^+$	$1.00 \times 10^{-9} \exp(-464/T)$	3

REFERENCES.— (1)Haiman, Thoul, & Loeb 1996; (3) Galli & Palla 1998.

TABLE 3
PARAMETERS FOR THE DIFFERENT RUNS

	M/M_\odot	z_{vir}	n	ω	Ω_B	HD	N_{SPH}
Run A	2×10^6	30	-3	0.2	0.05	Yes	16384
Run B	2×10^6	30	-3	0.2	0.05	Yes	131072
Run C	2×10^6	30	-3	0.1	0.05	Yes	16384
Run D	2×10^6	30	-3	0.4	0.05	Yes	16384
Run E	2×10^6	30	0	0.2	0.05	Yes	16384
Run F	2×10^6	30	-3	0.2	0.05	No	16384
Run G	2×10^6	20	-3	0.2	0.05	Yes	16384
Run H	2×10^5	30	-3	0.2	0.05	Yes	16384
Run K ^a	2×10^6	30	-3	0.2	0.05	Yes	16384
Run L	2×10^5	30	-3	0.2	0.20	Yes	16384

^aRun K has the same parameters as Run A, but with a different realization of the random density field.

NOTE.— n is the spectral index, ω the dimensionless angular velocity, Ω_B the baryon fraction, and HD refers to the absence or presence of HD cooling.

TABLE 4
EFFICIENCY OF FORMING CLUMPS

	t_{dyn} [yr]	M_{cool} [M_\odot]	$\langle M_J \rangle$ [M_\odot]	f_{Cl}
Run A	6.0×10^6	8.0×10^4	3.0×10^4	0.5
Run C	5.4×10^6	9.0×10^4	2.0×10^4	0.7
Run E	3.0×10^6	8.5×10^4	1.5×10^4	0.7

NOTE.—Parameters for the simulations in Figure 21. t_{dyn} is the dynamical time of the DM halo at the moment of virialization, M_{cool} the total amount of gas which has been able to cool, $\langle M_J \rangle$ the average Jeans mass at virialization, and f_{Cl} the baryonic mass fraction in clumps. Run K has virtually the same parameters as Run A.

TABLE 5
 EXPECTED MERGING OF CLUMPS

	n_{Cl} [pc ⁻³]	v [km s ⁻¹]	t_{coll} [yr]	N_{merger}
Run A	5×10^{-3}	12.3	1.5×10^7	~ 1
Run C	3×10^{-2}	10.3	3.0×10^6	~ 5
Run E	3×10^{-2}	14.3	3.0×10^6	~ 5

NOTE.—Explaining the merging histories in Figure 21. n_{Cl} is the number density of clumps, v the velocity dispersion, t_{coll} the collision timescale, and N_{merger} the expected number of mergers in $\Delta t \simeq 2 \times 10^7$ yr. Run K has virtually the same parameters as Run A.